Effects on Target Geology

Auriol S. P. Rae[1*] and Veronica J. Bray[2]

[1*]*Department of Earth Sciences, University of Cambridge, Cambridge, UK.*

aspr2@cam.ac.uk

[2]*The Lunar and Planetary Laboratory, University of Arizona, Tucson, Arizona 85721, USA.*

This manuscript has been submitted for publication as a book chapter in *Impact Cratering Across the Solar System (Volume eds. Catherine Neish and Gordon Osinski*; *Series eds. Paul Byrne, Rosaly Lopes, and Matt Siegler*) to be published in the Elsevier S&T Book Series. This manuscript has been reviewed by the Volume Editors. Subsequent versions of this manuscript may have revised content. Upon final acceptance of the book for publication, the final version will be available via the '*Peer-reviewed Publication DOI'* link on the right-hand side of this webpage. Please feel free to contact any of the authors; we welcome feedback.

Abstract

The process of impact crater formation can fundamentally change the nature of target materials, creating products that can be observed from planetary-scale geophysics all the way down to mineral microstructure. Impact-generated shock waves can vaporise, melt, and permanently deform the materials they pass through. Large quantities of the target are damaged and displaced, ejecting material outside of the crater and redistributing various shock products and brecciated material within the crater. The aim of this chapter is to describe the changes that occur within target materials and the physical processes that produce them during an impact event.

Effects on Target Geology

Auriol S. P. Rae[1] and Veronica J. Bray[2]

[1]*Department of Earth Sciences, University of Cambridge, Cambridge, UK.*

[2]*The Lunar and Planetary Laboratory, University of Arizona, Tucson, Arizona 85721, USA.*

Introduction

The process of impact crater formation can fundamentally change the nature of target materials, creating products that can be observed from planetary-scale geophysics all the way down to mineral microstructure. Impact-generated shock waves can vaporise, melt, and permanently deform the materials they pass through. Large quantities of the target are damaged and displaced, ejecting material outside of the crater and redistributing various shock products and brecciated material within the crater. The aim of this chapter is to describe the changes that occur within target materials and the physical processes that produce them during an impact event. Here, we include a description of the crater formation stages as they relate to the production of changes in the target geology.

This chapter is structured in terms of the processes that affect the geology of the target. We begin with a description of shock waves, followed by a description of how crater excavation and modification displace and deform the target. We then describe the specific and identifiable effects of crater formation on the target geology over a range of scales that can be utilised for the study of impacts on Earth. Finally, we describe the geophysical signature of impact craters, as seen from orbiting spacecraft.

Shock Wave Processes

In this section, the basic concepts of shock physics and their effects on target geology are described, including: vaporisation and melting of target rocks, solid-state shock metamorphism, and more general rock failure. For a more detailed description of shock physics, see Melosh (1989).

Stress Waves and Yielding

When an impact occurs, energy is transferred into the target and impactor in the form of a stress wave: a fluctuation of pressure, density, and particle velocity that propagates away from its source (**Figure 1**). Stress waves in solids are more generally familiar in the form of seismic waves. Here, we shall focus on one specific type of seismic wave: compression waves. Compression waves, also called "Pressure" or "Primary"-waves (P-waves) when referring to earthquakes, involve the particles in the solid oscillating along the same axis as the direction of the wave movement. In a compression wave, the direction of maximum compression is longitudinal, i.e. parallel to the propagation direction. The direction of minimum compression is transverse, i.e. perpendicular to the propagation direction.

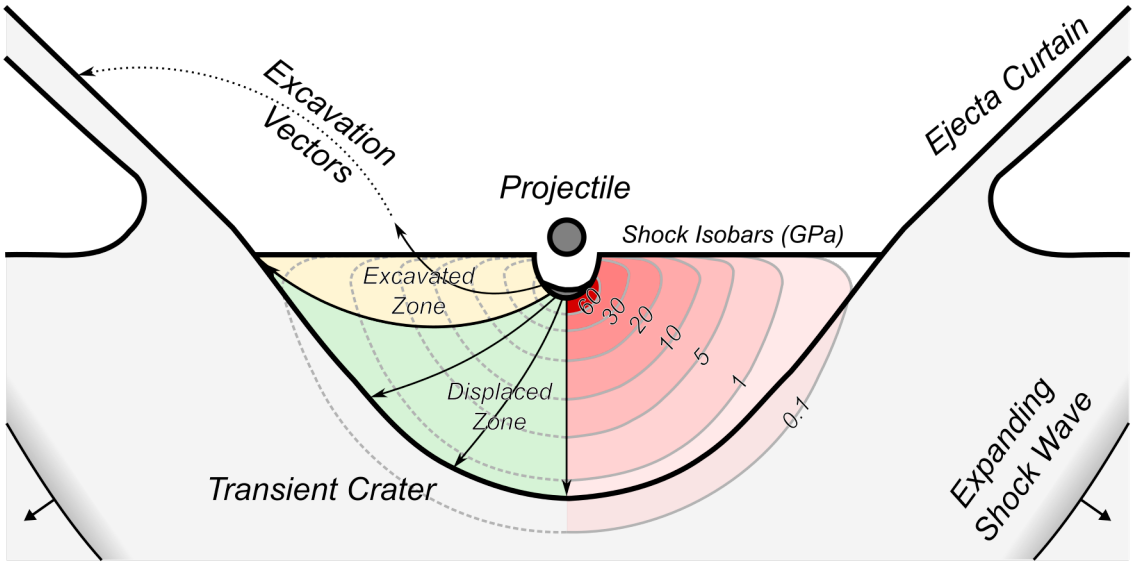

Figure 1: Schematic diagram of impact crater formation. A projectile travelling at a high velocity strikes the target generating a shock wave which expands into the target. Material is set in motion by the shock wave producing impact ejecta and moving the target downwards and outwards to create the transient crater. Based on Kenkmann et al. (2014).

The longitudinal stress in a compressional wave is always greater than the transverse stress. As the amplitude (the maximum distance of a particle's oscillation as measured from its equilibrium position) of a P-wave increases, both the longitudinal and transverse stresses increase, however, transverse stresses increase at a slower rate, and thus differential stress, i.e. the difference between the longitudinal stress, $\sigma_{L,}$ and transverse stress, σ_T, increases. Solid geological materials can resist extremely large pressures but their ability to resist differential stresses is limited. At a critical amplitude of a compressive wave, the state of stress exceeds the yield criterion of the material (**Figure 2**). Below this critical stress, the deformation of the

material is recoverable, i.e. elastic. Above this critical stress, the deformation is permanent, i.e. plastic, and can be seen in the geological record. This critical stress is known as the Hugoniot Elastic Limit (HEL).

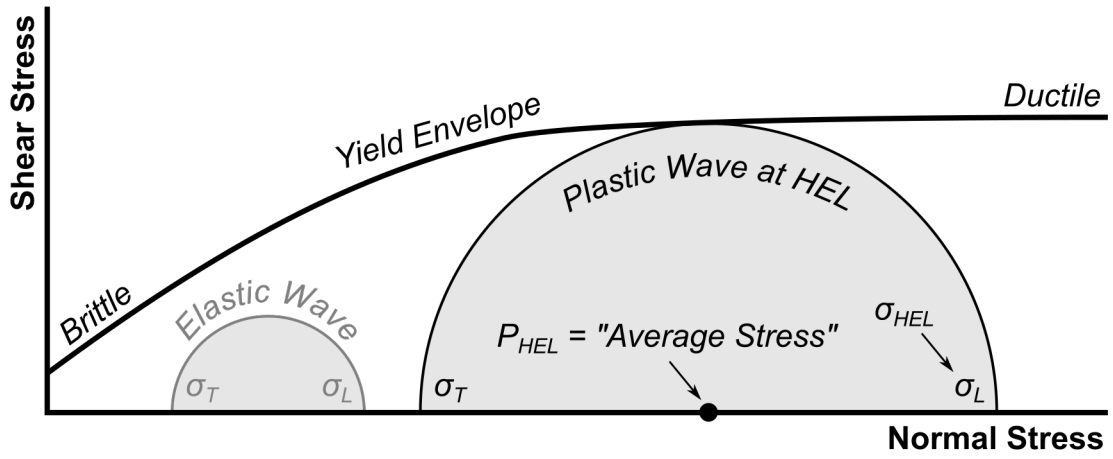

Figure 2: Mohr's circle representation of stresses within an elastic wave below the Hugoniot Elastic Limit (HEL). and a plastic wave at the HEL. The "yield envelope" describes the critical states of stress required to cause permanent deformation in the material. The Mohr circles, centred along the normal stress axis, represent the state of stress in the material. The state of stress in an elastic wave lies entirely within the failure envelope, thus does not cause permanent deformation to the material. However, as the amplitude of a stress wave increases the difference between σ_L and σ_T increases such that the Mohr circle intersects the yield envelope causing plastic yielding of the material, which may be accommodated by brittle or ductile deformation mechanisms. The critical state where the stresses in a wave reach the yield envelope is the HEL.

Plastic and Shock Waves

The speed of an elastic wave is constant in a given material, though it varies between materials. Once plastic yielding has occurred, the velocity of the wave – now a plastic wave - is near to the bulk sound speed of the material, which is lower than the original elastic wave speed (**Figure 3**). The velocity of a plastic wave increases with the amplitude of the stress wave because of the changes in physical properties that occur with increasing pressure. A plastic wave is termed a shock wave once its velocity exceeds the elastic wave speed, however, in geological literature and henceforth in this text, all plastic waves are known as shock waves because they cause permanent deformation in the materials they pass through (**Figure 3**).

As a result of the increase in velocity with amplitude that occurs in plastic waves, so-called “non-linear behaviour”, the fronts of shock waves are steep, almost instantaneous jumps from the initial state to a final state. At this instantaneous jump, properties such as density, velocity, internal energy, and others will increase. The conditions on either side of a shock can be estimated using a combination of the Rankine-Hugoniot equations and an Equation of State, specific to the material through which the wave is travelling. Use of these equations allow the pressure of the shock waves to be determined algebraically. The changes initiated in a target in response to an impact depend on the maximum shock pressure in the target as it determines the highest grade of shock metamorphism features that can occur in the target material.

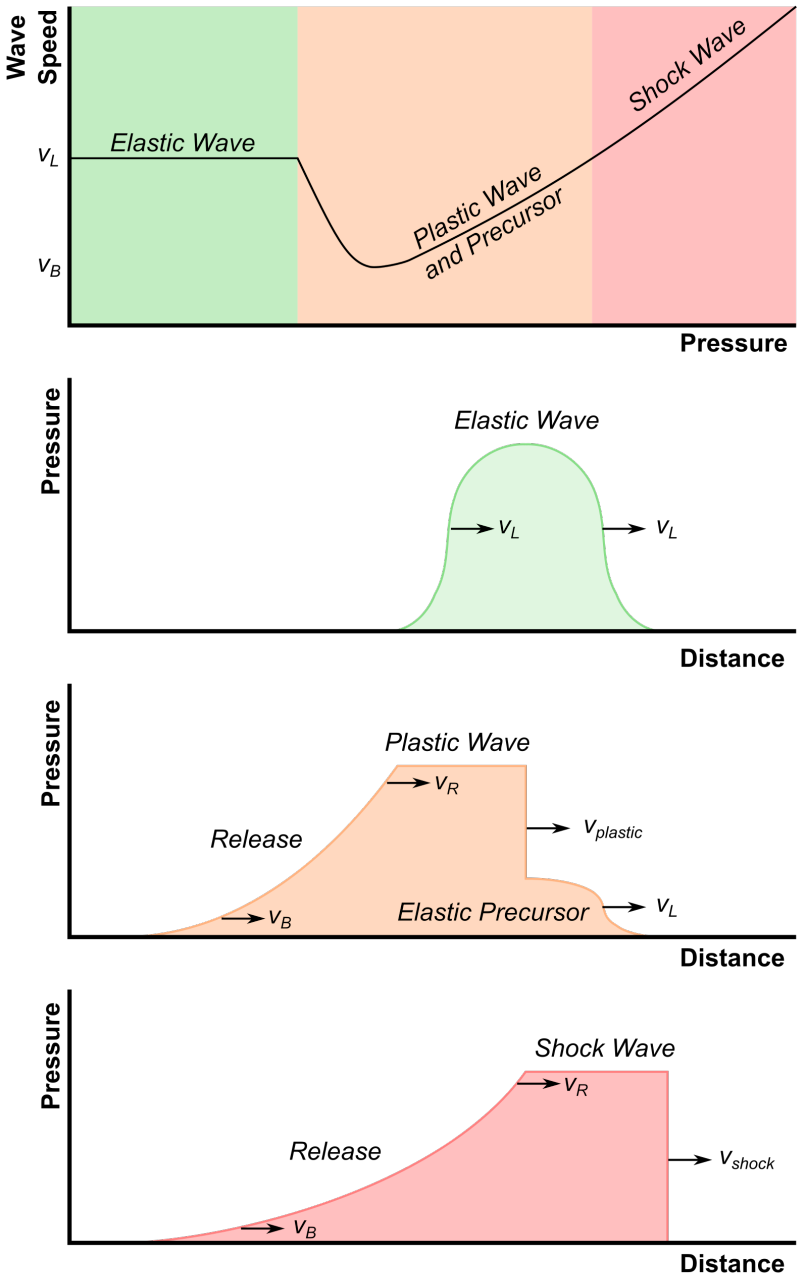

Figure 3: The velocity and structure of high amplitude stress waves. a) The propagation velocities of stress waves as a function of the pressure in the wave. Longitudinal elastic body waves travel at a constant velocity, V_L, otherwise known as the P-wave velocity. Stronger waves break into an elastic wave and a plastic wave that travels at a lower velocity, $V_{plastic}$, which may be as low as the bulk sound speed V_B. At even higher pressures, the velocity of the shock wave V_{shock} exceeds V_L and so there is no elastic precursor. b), c), and d) show the three distinct forms of stress wave: elastic, plastic with an elastic precursor, and shock respectively. The release of high pressures in a shock wave occurs due to the propagation of rarefaction waves. The velocity of these waves depends on the pressure of the material they propagate through, with minimum velocity of V_B, and maximum velocity V_R which are always larger than $V_{plastic}$ or V_{shock}. With distance from the point of an impact, proximal regions of the target will experience a true shock wave, greater distances will experience a plastic wave with elastic precursor, and distal locations will experience an elastic wave. Modified from Melosh (1989).

Attenuation of Shock

Peak shock pressure at the impact point is controlled by impact velocity, target density, impact angle, etc. However, the produced shock pressure calculated at a given distance from the impact point is influenced by additional factors that remove energy from the shock wave; including the radial spreading of the shock wave, loss of energy to heating, closing of pore space, and acceleration of the target, etc.

The contact point between the impactor and the target, at the point of impact, is commonly approximated as a "free surface". A free surface is, by definition, an interface of zero pressure. When the high-pressure shock wave arrives at the free surface of both the projectile and target, a rarefaction wave that releases shock pressures is generated to satisfy this condition (see Figure 3). The rarefaction wave propagates downwards, into the target, releasing rocks from the shock state. Rarefaction waves travel at the bulk sound speed of the material they pass through, however, as they propagate into highly compressed material, the front of the rarefaction wave travels at a velocity greater than the shock wave velocity

The trailing end of the rarefaction wave, where pressures approach ambient conditions, travel at a slower velocity near to the elastic bulk sound speed. Consequently, where the rise of a shock wave is almost instantaneous, shock release is a gradual process that occurs over an increasingly large period of time as distance from the impact point increases. Additionally, locations close to the point of impact experience a plateau in peak shock pressure behind the shock front but before the arrival of the rarefaction wave, a so-called "isobaric core" (**Figure 3)**. As the rarefaction wave travels faster than the shock front, the isobaric core disappears as the time of peak shock pressure also corresponds to the arrival of the rarefaction wave. This typically occurs at distances within one to two impactor diameters of the point of impact.

The rarefaction wave is one of the causes of shock attenuation, the decrease in peak shock pressures that occurs with increasing distance from the point of impact. This leads to progressively lower-grade shock-metamorphism as distance from the impact point increases (**Figure 1**). Beyond the isobaric core, peak pressure, *P*, decays rapidly from the impact point according to the power law (**Figure 4**):

Equation 1

$$P = P_{max}\left(\frac{L}{r}\right)^{n},$$

where P_{max} is the peak pressure developed in the isobaric core at the point of contact and compression, L is the impactor diameter, r is radial distance from the point of impact, and the exponent, n, takes a value from ~1.5 – 4, that depends on impact velocity (Ahrens and O'Keefe, 1987; Pierazzo et al., 1997), impact angle (Pierazzo and Melosh, 2000a), and azimuth within the target (Dahl and Schultz, 2001). Numerical simulations suggest that an average value of 1.933 ± 0.181 can be used for all impacts that hit at an angle steeper than 30° (Pierazzo and Melosh, 2000a).

Shock isobars, surfaces that connect materials that experienced the same peak shock pressure, are arranged concentrically around the transient cavity. The most highly shocked rocks line the floor of the cavity and progressively less shocked rocks are found at greater depths beneath the transient cavity surface (**Figure 4**).

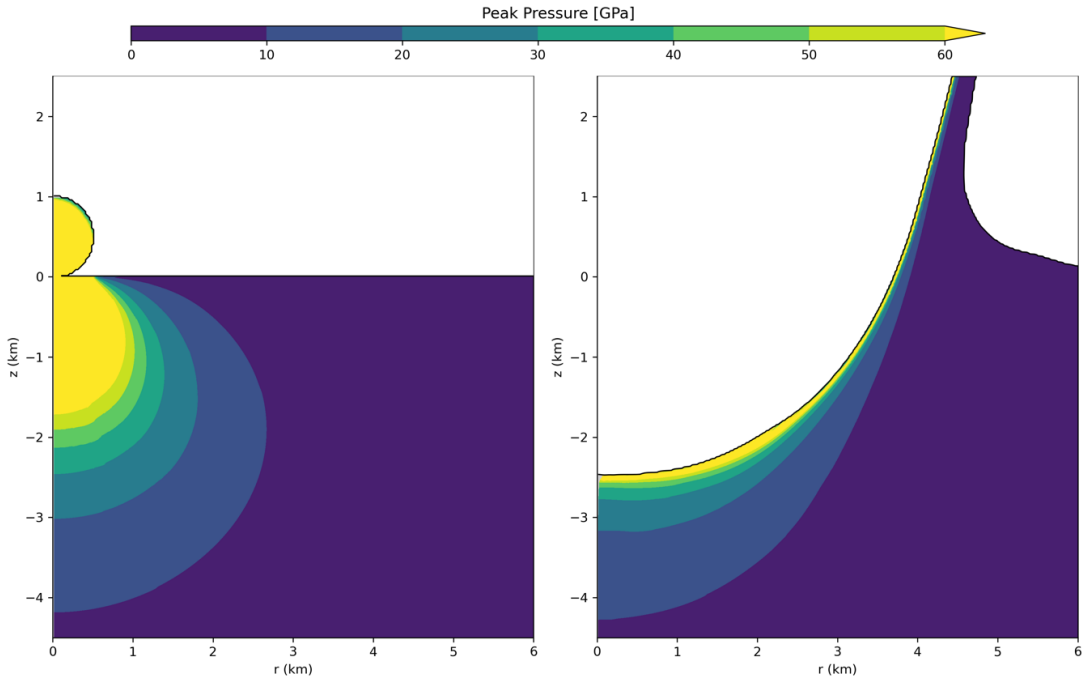

Figure 4: Distribution of shock isobars represented a) at the initial locations of material in the target – a provenance plot, and b) within the transient crater, at which time, the target has deformed such that shock isobars are approximately concentric to the wall of the transient crater.

Melting and Vaporization

Shock compression is a nearly instantaneous and thermodynamically irreversible process. Release from the state of shock is a gradual and thermodynamically reversible process. The energy increase during compression is always greater than the energy decrease during release. Consequently, rocks always have greater internal energy after they have been shocked than they had before they were shocked, and a post-shock temperature that is greater than the pre-shock temperature. The internal energy controls the phase of the post-shock material.

One significant consequence of the increase in energy due to shock compression and release is melting and vaporisation of the material (**Figure 5**). This is controlled by the magnitude of the shock wave because, for a given material, there is a critical shock pressure at which the total energy increase due to shock compression and release is enough to cause melting by the time the material returns to ambient pressures. In rocks, melting and vaporisation most commonly occurs during shock release, rather than during pressure rise or at peak pressure. Once melting has occurred, continued decompression may result in partial vaporisation. If the release adiabat passes through or above the critical point, complete vaporisation will occur. **Table 1** provides shock melting and vaporisation criteria for a variety of common planetary and geological materials.

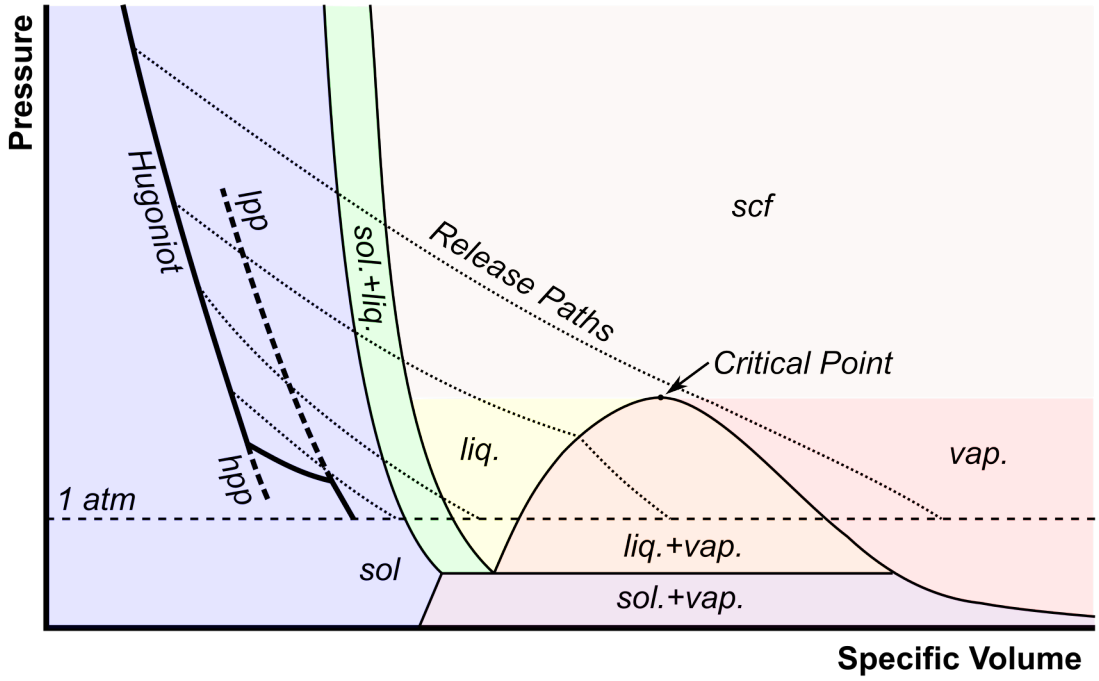

Figure 5: Shock melting and vaporisation during release from shock in a hypothetical silicate mineral. The Hugoniot curve (thick black line) represents the locus of all shock states, the kink at low pressures is caused by a phase change from a low pressure phase (lpp) to a high pressure phase (hpp). During rarefaction, material follows release adiabats (thin dotted lines) back to ambient pressure conditions (1 atm). These release adiabats may cross phase

boundaries (black lines) in the material such that, upon release being complete, the material may remain solid (sol.) or have partially or wholly become liquid (liq.) or vapour (vap.) – potentially transitioning to a super-critical fluid (scf) during decompression. The final state of the material depends upon what point on the Hugoniot the material was originally shocked to, thus melting and vaporisation criteria are defined by a given shock pressure. Modified from Ahrens and O'Keefe (1972).

Table 1: Pressure criteria of shock melting and vaporisation in common planetary materials. Unless otherwise specified, all materials are assumed to be at standard conditions in the pre-shocked state.

Material	***Melting (GPa)***		***Vaporisation (GPa)***		
	Incipient	**Complete**	**Incipient**	**Complete**	
Granite	46	56	140	1265	Pierazzo et al. (1997)
Basalt	96	115.5	205.5	>1138	Pierazzo et al. (2005)
Calcite	-	-	66*	-	Wünnemann et al. (2008)
Anorthosite	43	52	102	590	Ahrens and O'Keefe (1977)
Forsterite	-	189	270	856	Davies et al. (2020)
Quartz	-	57.6	90.9	260	Kraus et al. (2012)
*Water/Ice (50K)***	2.1	4.0	4.0	70.4	Kraus et al. (2011)
*Water/Ice (150K)***	1.6	3.5	3.5	69.6	Kraus et al. (2011)
*Water/Ice (250K)***	0.5	2.7	2.7	66.9	Kraus et al. (2011)
Iron	218	263	468	3507	Stewart et al. (2020)
Aluminium	73	106	315	-	Pierazzo et al. (1997)

** These pressures indicate the onset of calcite decarbonation, $CaCO_3$ -> $CaO + CO_2$, rather than vapourisation.*
*** The onset of vapourisation for ice depends upon the partial pressure of the environment into which the shocked material expands. The tabulated pressure is the pressure from which the release adiabat passes through the critical point.*

The amount of impact melt generated by a given impact can be determined from the following scaling relationship (Pierazzo and Melosh, 2000b, Wünnemann et al., 2008):

Equation 2

$$\frac{M_m}{M_i} = k\left(\frac{{v_i}^2}{\varepsilon_M}\right)^{\eta} \sin^{1.3}\theta,$$

where M_m and M_i are the masses of impact melt and impactor respectively; θ is the impact angle; η is a constant that takes a value between 0.5 and 1, a value of 1 indicates that melt mass scales with impact energy while a value of 0.5 indicates that melt mass scales with impactor momentum; ε_M is the critical energy required for melting, determined as the energy on the Hugoniot where adiabatic release to 1 bar results in complete melting; and k is an empirical constant. The values of η, ε_M, and k vary depending on material (**Table 2**); the values are determined from a combination of laboratory measurements and shock physics and thermodynamical modelling. Vapour scaling follows a similar relationship as a function of

velocity, but with varying parameters. A useful rule of thumb is that the mass of vapour is ~10% of the melt mass. In crater scaling relationships, impact melt volumes scale with velocity with a larger exponent (~1.7-2) than the volume of the transient cavity (1.3). Thus, the volume of impact melt becomes progressively more significant to the structure of a crater with increasing size (Grieve and Cintala, 1992; Cintala and Grieve, 1998).

Table 2: Impact melt scaling parameters (Wünnemann et al., 2008).

Material	ε_M *(MJ/kg)*	k	η
Non-porous rock	3-6	0.14	1
Porous rock	2-4	0.25	0.85
Ice (at 125 K)	0.8	0.5	0.83

Impact heating can have a profound effect on the physical properties of the target material: affecting the magnetic properties of rocks, driving hydrothermal activity, resetting geochronometers, and allowing for the formation of economic deposits. The distribution of that heat energy is generally concentrated close to the centre of the impact crater, and close to the surface. The distribution of impact melt products is affected by excavation and modification processes during crater formation. Most melt will remain within and around the crater as distinct melt deposits and as a component of impact melt-bearing breccias, while some molten and vaporised products such as tektites and spherules can be ejected to great distances from the source crater.

Post-Shock Processes

Impact cratering is a large-scale geological process, involving the sudden application of large stresses (see **Section 4.1**). The corresponding amount of differential stress experienced by the target material leads to failure of the rock mass over a large area. Impact craters are thus associated with regions of high fracture density, brecciation and significant displacement of material from its original position. As with the last section, we describe only the portions of the crater excavation and modification stages that are useful for the explanation of changes in target geology.

Excavation

The passage of the shock wave accelerates material outwards, away from the point of impact, resulting in the excavation of a transient cavity and the formation of ballistically emplaced ejecta.

The excavation flow of material leads away from the impact point, moving outwards (Maxwell, 1977). The flow paths cut shock isobars, delivering both high and low-shock material outwards along the same flow path. Zones of material in the excavation flow are commonly described by diagrams such as **Figure 1**, where material is subdivided into an "excavated" zone and a "displaced" zone. The excavated zone marks contains all material that ultimately ends up outside the transient crater rim. All material in the displaced zone undergoes extreme deformations, which for brittle materials results in fragmentation, brecciation, and fracturing. The displaced zone can also include a large quantity of melt.

The rim of the transient cavity can be thought of as a critical point that divides material moving out and away from the crater, and material destined to fall back into the crater cavity. Once the material that is being ejected has risen above the pre-impact surface, the diverging flow paths of this material away from the impact point will result in separation of ejecta into non-coherent blocks that begin to follow ballistic trajectories. In general, the highest velocity ejecta will be deposited at the greatest distances from the crater and contain the largest proportion of highly shocked material in the ejecta deposits. The lowest velocity ejecta over-turns to form the crater rim – resulting in the reversal of local stratigraphy (**Figure 6**). Together with the emplacement of ejecta as an overturned rim flap, deformation beneath the surface of

the transient cavity, e.g. intrusions of breccia dikes, causes uplift to the rims of craters. The structural uplift may contribute up to ~70-80% of the topographic elevation at crater rims in both simple and complex craters (Sharpton, 2014; Sturm et al., 2016; Krüger et al., 2017). The topographic contribution of structural uplift decreases to zero within 1.7 transient crater radii, at which point the ejecta provides the main source of post-impact elevated terrain around the crater (Shoemaker, 1963; Roddy, 1977).

Modification

We note here that modification serves as another source of breccia creation and large-scale transportation of material. In general, crater collapse occurs when gravitational forces overcome the strength properties of the material. The extent of crater collapse is controlled by the size of the crater, the target body gravity, and the strength of the material being impacted. Larger craters undergo more significant modification of the transient cavity, creating complex crater morphologies. Small transient cavities generally modify to relatively simple, bowl-shaped craters. Observations from drill cores of the Brent and Barringer craters demonstrate that the floors of simple craters are filled with a lens of brecciated rocks. The breccia lens of a simple crater can contain material of all stages of shock metamorphism; from unshocked to melted. The origin of the breccia lens results from debris sliding from the rim of the transient crater into the crater floor to form a deposit of breccia above the fractured and minimally displaced “true” crater floor. This acts to increase the diameter and decrease the depth of the final crater. The process of breccia lens formation involves partial collapse and erosion of the uplifted transient crater rim, however the rims of simple craters after modification are still local topographic highs.

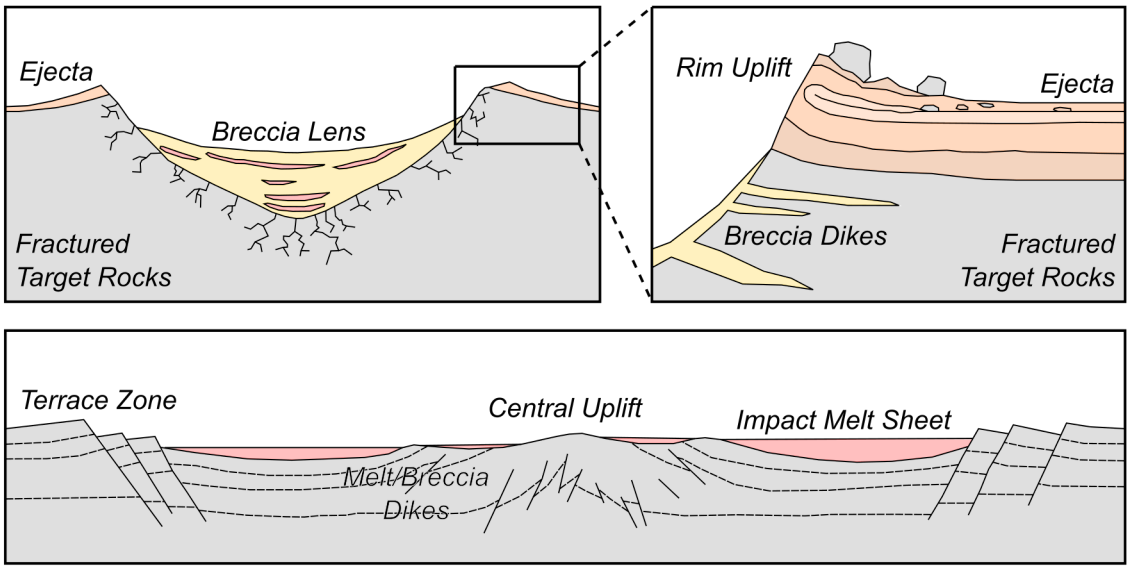

Figure 6: Schematic cross-sections of simple and complex impact structures. Based on Grieve (1987) and Melosh (1989).

Complex craters possess terrace zones interior to the final crater rim (**Figure 6**). The width of these terraces decrease with distance inside the crater before reaching a flat-lying crater floor. The terraces of complex craters are the surface expression of sequential fault blocks, where the steep, inwardly dipping scarps between terraces are the exhumed footwalls. The terrace zone is therefore an expression of the same kinematics as breccia lens formation in simple craters, where the walls of the transient cavity collapse inwards towards the crater centre. The difference, however, is that terrace zones are composed of coherent rock masses being displaced along faults, rather than incoherent rock fragments.

The stratigraphic uplift of material during the modification of large transient cavities brings deep material to the surface. This transport results in a central peak, or other central morphology, exposing sometimes unique mineralogies at the surface. The maximum stratigraphic uplift expressed in the centre of complex craters is approximately equal to 10% of the final crater diameter (Melosh and Ivanov, 1999). For large enough craters, stratigraphic uplift can incorporate dense mantle material beneath the crater, as identified at Chicxulub (Christeson et al., 2009) and in lunar impact basins (Neumann et al., 1996).

In addition to the uplift of deep crustal, or even mantle material beneath the centre of impact structures, exhumation of sub-surface material also occurs on icy bodies by impacts that partially or fully penetrate a solid ice crust. Large central pit craters on Ganymede, Callisto and Ceres are partially to completely filled with bright, sub-circular domed deposits. Central-

dome and anomalous-dome craters are hypothesised to form from deeply penetrating impacts exposing a relatively fluid layer beneath a brittle ice crust. Warm subsurface ice then rises to the surface in the crater centre and freezes to form a dome of fresh ice (Schenk, 1993). A large enough impact will fully penetrate the ice crust, exposing sub-surface oceans and bringing fluid to the surface of those bodies. At this size, impacts affect a larger portion of the surrounding crust than the region directly excavated by the impact, forming multiple external ring structures – multi-ring basins. The largest multi-ring system in the solar system is Valhalla on Jupiter's moon Callisto. The rings of the Valhalla system are structurally different from those at the Lunar multi-ring basin Orientale, consisting of sets of outward-facing scarps and horst-graben sets, formed as brittle crust deforms above the sub-surface ocean in response to the impact event.

Physical Changes to the Target as a Result of Impact

So far in this chapter, the displacement and deformation experienced by target materials during shock compression, crater excavation, and crater modification have been described. The net result of all of these processes is that target materials can have substantially different properties after impact than they had initially. These changes can be observed from remote geophysics down to the microscopic scale. In this section we will describe the consequences of impacts on the properties of target materials. First, we will describe how shock metamorphism is manifested in target rocks. Then, we will describe the physical properties of materials within impact structures and the processes that produce these properties. The mixing of shock products and brecciation in the target, and their subsequent modification, results in complex impact products that cannot be simply prescribed to shock-related or brecciation-related processes. Instead, these changes to target geology are presented separately, with explanation of the physical processes involved following.

Shock Metamorphism

At pressures below the critical pressure required to produce shock melting, shock waves, by definition, still induce irreversible deformation in the material they pass through. Individual minerals within a rock will respond in unique ways to a given shock wave. As such, all minerals have a unique and diverse inventory of so-called "shock effects". Some of these effects are unique to shock deformation and can be diagnostic of a narrow range of conditions.

The most well understood mineral, in terms of shock metamorphism, is quartz (Stöffler and Langenhorst, 1994; Grieve et al., 1996; French and Koeberl, 2010). Quartz displays a wide variety of shock effects which are primarily sensitive to the peak shock pressure that the mineral experiences. Quartz is also extremely useful from the perspective of impact cratering on Earth as it is extremely common within the Earth's crust and is geologically robust, i.e. it will commonly retain identifiable shock effects even after hundreds of millions of years.

Shock effects in quartz

At low shock pressures, quartz develops planar microstructures or ‘elements’, which are divided into planar fractures (PFs), feather features (FFs) and planar deformation features (PDFs). PFs and PDFs are crystallographically controlled, i.e. they are oriented parallel to rational crystallographic planes – planes defined by the symmetry of the crystal structure and the way ions in the structure are bonded. Belonging to the trigonal/rhombohedral crystal system, crystallographic planes in quartz are described by Miller-Bravais indices as shown in **Figure 7**.

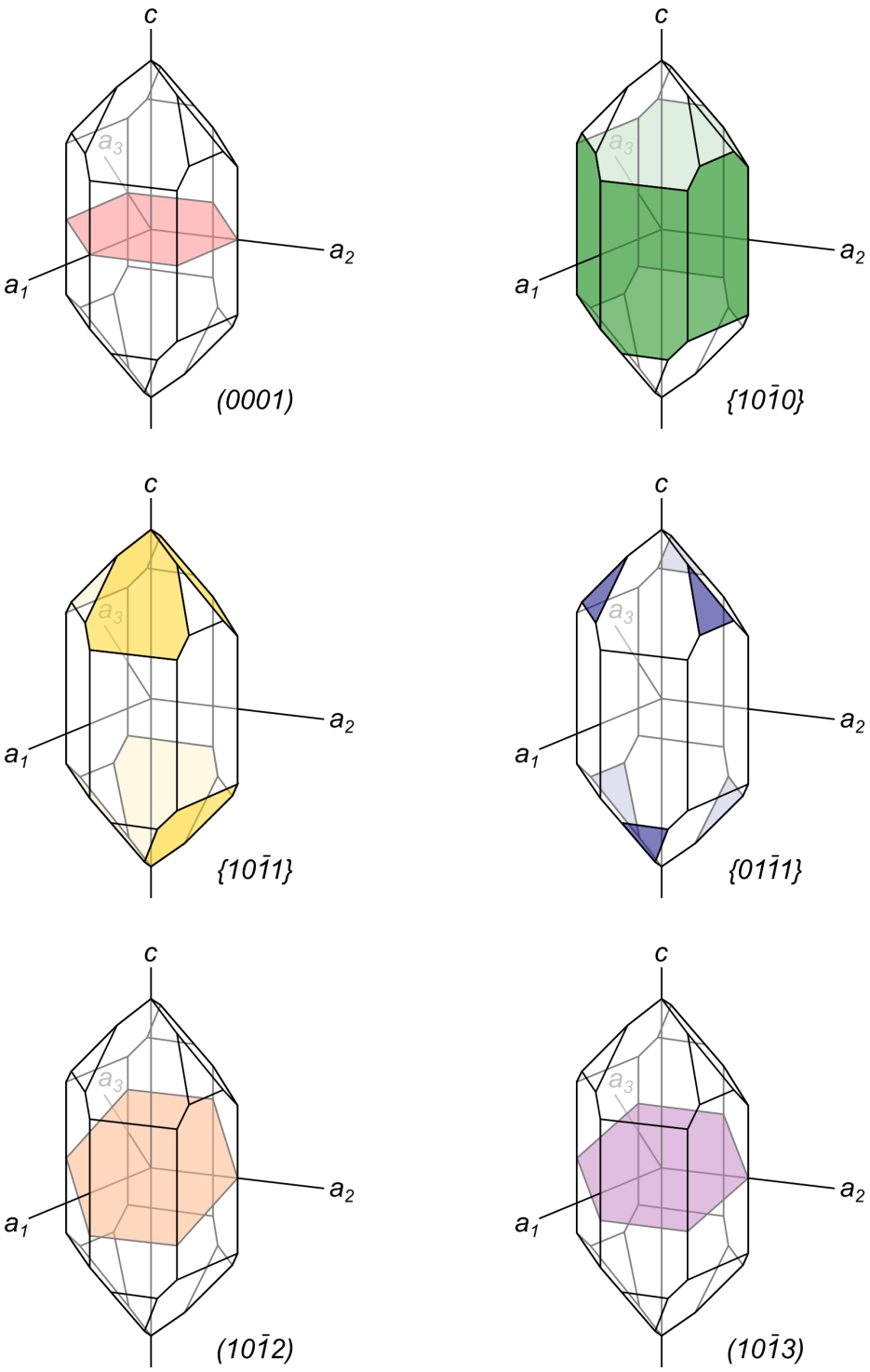

Figure 7: Crystallographic orientations in quartz. Each plane is described by the Miller-Bravais indices (hkil), {hkil} indicates the set of all planes that are symmetrically equivalent to (hkil). The indices h,k,i, and l denote the inverse intercepts along the lattice vectors a1, a2, a3, and c respectively: e.g., $(10\bar{1}3)$ *can be defined by a plane that intersects the a_1-axis at 1, the a_3-axis at -1 (negative indicated by the bar symbol), the c-axis at 1/3, and does not intersect the a_2-axis. Here, single planes are shown where either there is only a single equivalent plane in that orientation, e.g. (0001), or for diagrammatic simplicity.*

Planar Fractures (PFs) are crystallographically planar open fissures that commonly occur as parallel sets of multiple individual fractures. An individual PF is typically around 3 μm wide, and the spacing between PFs in a set is ~15-20 μm (**Figures 8a and 8b**). PFs commonly form sets that are parallel to the basal plane of quartz, (0001), but can be found in a variety of other rational crystallographic orientations. PFs can be observed in quartz grains that experience peak pressures greater than ~5 GPa, however they are not unique to shock metamorphism and can form as a result of endogenic, tectonic deformation. However, it has been claimed that quartz displaying PF sets in multiple crystallographic orientations within the same grain are a unique result of shock metamorphism (French and Koeberl, 2010).

Feather Features (FFs) consist of a single PF and a set of many thinly-spaced (1-4 μm), short (2-10 μm), sub-parallel, open fractures, that branch at an angle of at least 35° from the PF (**Figures 8e and 8f**) – These small fractures are known as "feather feature lamellae". The orientation of FF lamellae are, to a certain degree, crystallographically controlled, although their orientation within a sample tend to cluster around a single orientation, which has been suggested to indicate the direction of shock wave propagation. FFs can be observed in rocks that experience pressures of at least 7-10 GPa (Poelchau and Kenkmann, 2011).

Planar Deformation Features (PDFs) are closed planar microstructures – not open fissures like PFs. Individually, they are narrow (less than 2 μm wide) planes of glassy material, arranged in crystallographically planar, parallel sets spaced 2-10 μm apart (Stöffler and Langenhorst, 1994; Grieve et al., 1996). PDFs can fully or partially traverse the grains they are contained within (**Figures 8c and 8d**). It is commonly found that PDFs do not cross PFs, suggesting a temporal relationship where PFs form prior to PDFs and are thus over-printed upon PDF formation. PDFs generally occur in more than one orientational set per grain. PDFs can be "undecorated" or "decorated". Pristine PDFs are undecorated and are composed of amorphous glass. Decorated PDFs are the result of the annealing of undecorated PDFs, resulting in planes of densely packed fluid inclusions that retain their crystallographically controlled orientation. PDFs are oriented parallel to rational crystallographic planes (**Figure 7**). Shock recovery experiments have demonstrated that the orientation at which PDFs form is sensitive to the peak pressure of the shock wave (**Table 3**). PDFs in quartz are the primary basis for conducting shock barometry in impactites on Earth – i.e. assigning a shock pressure value experienced by a rock based on observations within a rock. This is achieved by measuring the crystallographic orientations of PDFs in a selection of quartz grains and, based on the

distribution of those orientations, a shock pressure for the rock is assigned. PDFs form at pressures that range between 5 – 34 GPa.

Minerals are reactive substances that respond to changes in temperature and pressure. At a given pressure and temperature, each mineral has an equilibrium stable state. At standard temperature and pressure (25 °C and 1 atm), SiO_2's equilibrium state is in the crystallographic structure known as α-quartz, known commonly as quartz. At different P-T states, other mineral structures may be thermodynamically favoured over the α-quartz structure. At high pressures, stable mineral structures tend to be more dense than the stable structure at low pressures. Minerals of the same chemical composition, but different crystal structure are known as polymorphs. Quartz undergoes phase transformations to high-pressure polymorphs, coesite and stishovite. Under equilibrium conditions, coesite is stable at pressures > ~2 GPa, and stishovite is stable at pressures > ~8 GPa. However, while SiO_2 may be more stable in the form of coesite or stishovite at high pressures, a direct transformation from quartz to a high-pressure polymorph is reconstructive, i.e. bonds in the crystal structure must be broken and reformed, and is therefore slow – too slow to occur as a direct phase transformation during shock. Instead, coesite and stishovite are generally found in close association with diaplectic quartz glass or PDFs. These non-crystalline forms of SiO_2 appear to mediate the phase transformation. Upon decompression high-pressure polymorphs are metastable, that is their equilibrium structure reverts to α-quartz. However, much as the transformation from low- to high-pressure polymorph, the reversion of high- to low-pressure polymorphs is limited by the speed of reconstructive phase transformations – the transformation can be so slow, particularly after temperatures have dropped, that high-pressure polymorphs can remain in the geological record for long periods of time. Coesite and stishovite can be found in rocks that have experienced at least 30 and 12-15 GPa respectively (Stöffler, 1984).

Table 3: Summary of shock metamorphic effects in quartz. Data from Stöffler et al., (2018), Grieve et al., (1996), and refs. therein.

Feature	*Peak Pressure Range*
Planar Fractures	~5 – 34 GPa
Feather Features	> 7-10 GPa
Planar Deformation Features	5-34 GPa
$c(0001)$	5 – 34 GPa
$r\{10\bar{1}1\}$	5 – 34 GPa
$\omega\{10\bar{1}3\}$	10 – 34 GPa
$z\{01\bar{1}1\}$, $\xi\{11\bar{2}2\}$, $\{22\bar{4}1\}$, *and others.*	~15 – 34 GPa

$\pi\{10\bar{1}2\}$	20 – 34 GPa
Diaplectic Quartz Glass	34 – 50 GPa
Lechatelierite	>50 GPa
Coesite	30 – 55 GPa
Stishovite	12 – 45 GPa

At pressures greater than ~34 GPa, quartz undergoes a transformation from an ordered crystalline state to an amorphous phase known as diaplectic glass. This is a solid-state transformation (without melting) that results in a low-density, glass phase – a solid that lacks the long-range order characteristic of crystals. The transformation to diaplectic quartz glass has been shown to be dependent on initial crystallographic orientation and initial temperature (Stöffler and Langenhorst, 1994; Grieve et al., 1996). Beyond peak pressures greater than ~50 GPa, but lower than the critical pressure for whole-rock melting, individual mineral melting can occur. The product of quartz melting is known as lechatelierite, which is glassy, flow-textured, and often vesiculated (containing gas-pockets or voids). Lechaterierite is not unique to shock metamorphism as it can also be found in fulgarites, a.k.a. “fossil lightning”, as a result of flash heating in quartz-bearing sand.

Thus far, all stated shock pressures for shock metamorphic effects in quartz are for single crystals or non-porous rocks. In porous rocks, the distribution of peak shock pressures is significantly more heterogeneous. Pore space closure as the shock wave passes results in local excursions to higher pressures and higher temperatures within the shock and after the shock wave has passed. Together this results in some “high-pressure” shock metamorphic effects being found in rocks that have experienced lower average shock pressures. For example, diaplectic quartz glass and the high-pressure polymorphs, coesite and stishovite, have been found in experimentally shocked sandstones that have experienced shock pressures of only 10-20 GPa (Kowitz et al., 2013; 2016).

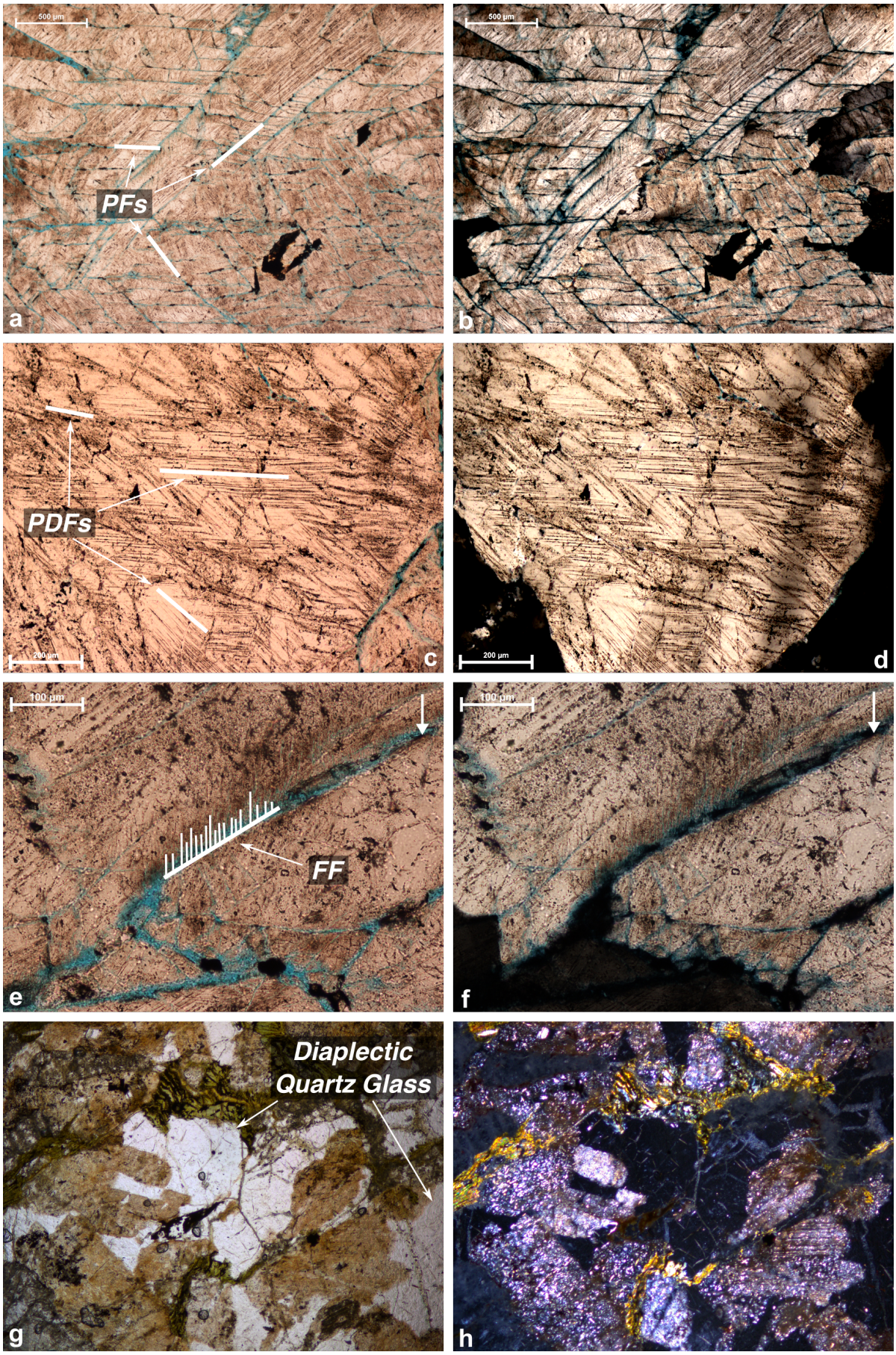
500 µm
PFs
a
500 µm
b
PDFs
200 µm
c
200 µm
d
100 µm
FF
e
100 µm
f
Diaplectic
Quartz Glass
g
h

Figure 8: Shock effects in quartz from: a-f) Site M0077 of the Chicxulub impact structure; g-h) Zipplingen quarry within the Ries impact structure. Planar fractures (PFs) in quartz under a) plane-polarised light (PPL) and b) cross-polarised light (XPL). Planar deformation features (PDFs) in quartz under c) PPL and d) XPL. Feather feature (FF) in quartz under e) PPL and f) XPL. Diaplectic quartz glass under g) PPL and h) XPL. Image Credit: Auriol Rae & Michael Poelchau.

Shock effects in other minerals

Many more shock effects can be found in other minerals (**Figures 9 and 10**), some of these effects are equivalent structures to those found in quartz. PFs form in olivine and zircon (Stöffler et al., 2018). PDFs have been observed in biotite, amphibole, pyroxene, olivine, plagioclase feldspar (**Figure 9c**), and alkali feldspar (**Figure 9d)** . All feldspars transform to diaplectic glasses prior to melting. Numerous minerals have high pressure polymorphs; examples include the transformation of graphite to diamond and lonsdaleite, the transformation of zircon to reidite (**Figure 9h**), and the transformation of olivine to wadsleyite and ringwoodite. A number of minerals also generate mechanical twins; notable examples of this include calcite, amphibole, and a variety of accessory phases such as zircon (**Figure 9g**), monazite, and titanite.

Some minerals do not possess shock effects that are unique to shock metamorphism. As a result, it is particularly challenging to identify shock metamorphism in some target rocks. On Earth, carbonate targets – which are common - are particularly challenging due to the lack of undisputed unique shock effects in calcite and dolomite. Furthermore, solid-state metamorphism in icy solids is generally less well understood than in silicates. However, similarly to silicates, ices can undergo a variety of phase transformations at high pressure, e.g., H_2O ice can transform to the high pressure ice VI–VIII phases. It remains to be seen how shock metamorphism in ices can be identified as shocked icy material generally melts, vapourises or returns to its low-pressure phase upon removal of shock conditions.

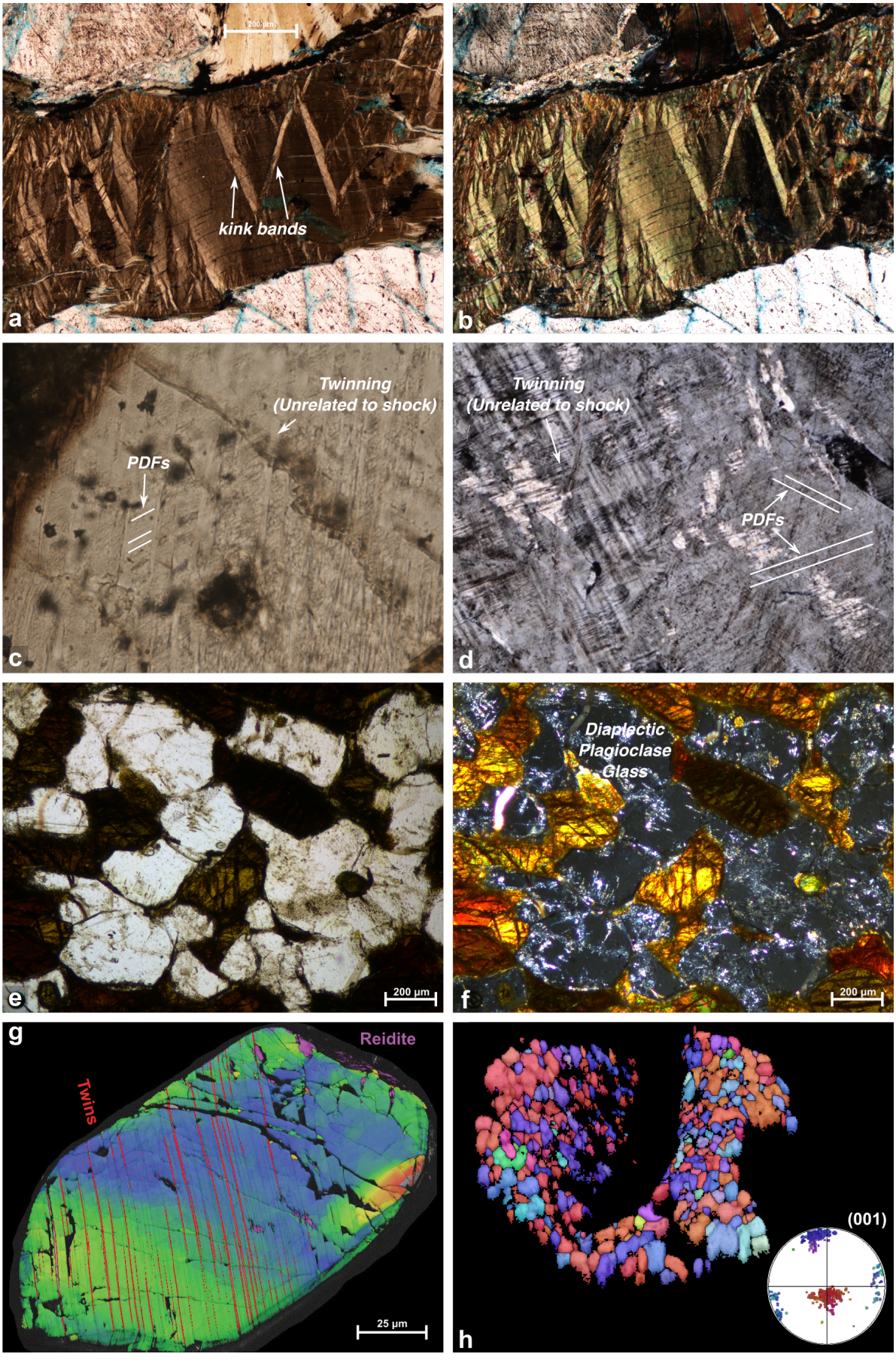
200 µm
kink bands
a
b
Twinning
(Unrelated to shock)
PDFs
c
Twinning
(Unrelated to shock)
PDFs
d
200 µm
e
Diaplectic
Plagioclase
Glass
200 µm
f
g
Reidite
Twins
25 µm
(001)
h

Figure 9: Shock effects in other minerals. a) and b) kinked biotite from Site M0077 of the Chicxulub impact structure, Mexico, in plane-polarised light (PPL) and cross-polarised light (XPL) respectively. c) PDFs in shocked plagioclase from Tenoumer impact structure, Mauritania under PPL, note that the PDFs only traverse one set of the lamellar twinning in plagioclase, twinning here is unrelated to shock (after Pickersgill et al., 2021). d) PDFs in shocked microcline (alkali feldspar), note that one set of PDFs is parallel to one of the twin sets, twinning here is unrelated to shock (after Pickersgill et al., 2021). e) and f) Diaplectic plagioclase glass from Alerheim within the Ries impact structure, in PPL and XPL respectively. g) Shocked zircon from the central uplift of the Woodleigh impact structure, Australia. The zircon contains irregular lenses of reidite that are offset by {112} shock deformation twins (after Cox et al. 2018). h) Granular zircon in an Australasian-field tektite from Thailand. The grain is former reidite in a granoblastic network (FRIGN) zircon, which means the neoblastic domains preserve systematic crystallographic orientation relations [see inset pole figure for (001)] that uniquely record the former presence of the high-pressure polymorph reidite (after Cavosie et al. 2018). Image credit: Auriol Rae, Annemarie Pickersgill, Michael Poelchau, and Aaron Cavosie.

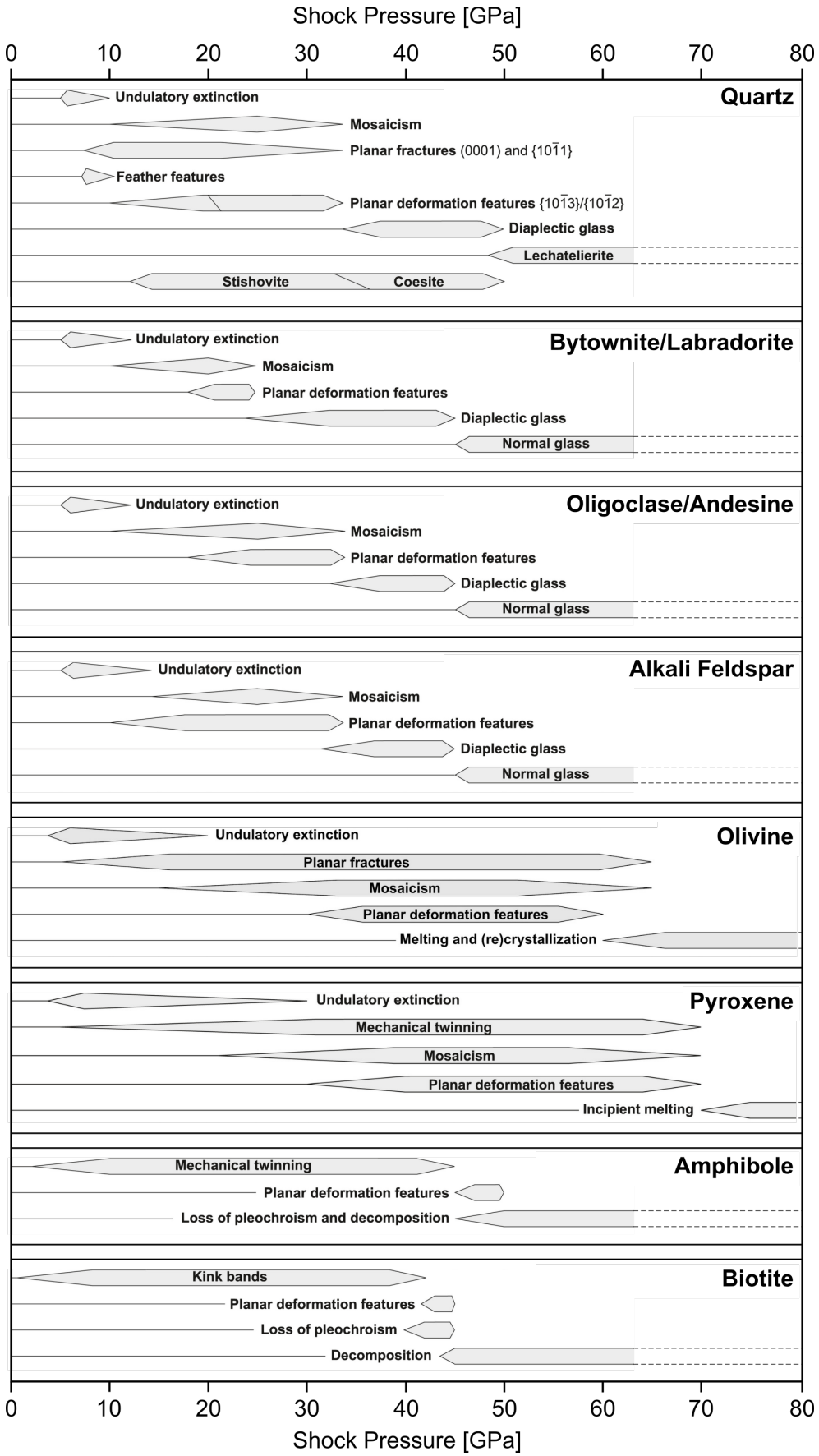

Figure 10: Summary of shock classification in a selection of rock-forming minerals. Adapted from Stöffler et al. (2018).

Fracturing and Shatter Cones

Beyond mineral specific shock effects, the passage of a shock wave results in the fracturing and brecciation of target rocks. In general, fracturing is not a diagnostic feature of shock; the exception to this rule is shatter cones. Shatter cones are striated conical fracture surfaces distinguished by their branching ridges distributed along the cone surface (**Figure 12**). Their formation mechanism is poorly understood, although it is generally interpreted that shatter cones point in the direction of maximum compression during shock metamorphism. While field studies at terrestrial impact structures (e.g. Dietz and Butler, 1964; Milton et al., 1996) have presented evidence that shatter cone orientations point towards a common point of impact, a number of more recent studies (Wieland et al., 2006; Osinski and Ferriere, 2016) have disputed this. Shatter cone orientations may instead respond to more local heterogeneities within the target rocks and thus reflection points of the shock wave.

Figure 11: Shatter cones from the Gosses Bluff impact structure. In this block, all shatter cone apices point downward, towards the bottom-right corner of the image.

Complexities of Shock Metamorphism

It is important to highlight that the formation mechanisms by which many of the shock metamorphic effects described above are poorly understood. Shock effects are commonly listed in terms of a given peak shock pressure required for formation (**Table 3, Figure 10**), but this is a simplification. First, most of the pressures given for specific shock effects assume that the material is at standard temperature and pressure before being shocked. The reason for this is simply that is harder to perform laboratory shock experiments at non-standard conditions. The consequence is that if initial temperatures are higher, lower shock pressures are required to cause melting and vapourisation. Additionally, higher initial temperatures have demonstrated effects on solid-state shock metamorphism: In quartz, initial temperature affects the distribution of PDF orientations generated at the same shock pressure, and the required shock pressure for complete transformation to diaplectic glass (Langenhorst and Deutsch, 1994). Varied initial conditions are likely to have similar consequences for the shock metamorphism of other minerals but, at this time, insufficient experimental results limit the quantification of these effects. Second, shock pressures themselves are not the direct cause of all solid-state shock metamorphism. Mineral twinning, for example, requires high differential stresses, rather than simply a high pressure, and is sensitive to temperature and strain rate (Christian and Mahajan, 1995). Furthermore, the orientations of PDFs in quartz have been shown to be sensitive to the relative orientation of crystallographic axes to the shock direction (Langenhorst and Deutsch, 1994), suggesting that PDF formation in a given orientation requires differential stresses acting in conducive orientations as well as high average stresses (i.e., pressure). Finally, proposed formation mechanisms of both FFs (Poelchau and Kenkmann, 2011) and shatter cones (Sagy et al., 2002; Baratoux and Melosh, 2003) suggest sensitivity to the orientation of stress during shock metamorphism. Today, it is increasingly clear that individual shock metamorphic effects in rocks and minerals are a complex manifestation of the initial conditions of the material and the history of applied stress during shock, albeit a “history” that last only seconds (Rae et al., 2021).

Physical properties of the Target: Density Modification

Impact cratering can lead to permanent density changes in the subsurface. Those processes are: dilatancy, tensile fracturing, compaction, hydrothermal activity, and uplift.

Tensile Failure

When a shock wave interacts with the free surface of the target or impactor a rarefaction wave is generated. Locations deep within the target first experience compression from the shock wave, and then experience tension as a result of the rarefaction wave. Close to the free surface, the rarefaction wave can arrive before the pressure rise in the shock front is complete; this area is known as the *interference zone* (**Figure 12**). Material in the interference zone experiences significantly lower peak pressures than would be predicted from radial attenuation from a point source. The tensile strength of rocks is generally low compared to their compressive strength. Therefore, the tensile stresses that develop within the interference zone can cause tensile failure of the rocks. Target rocks lying at shallow depths can therefore detach from the surface as *spall*.

Tensile stresses are not limited to the near-surface interference zone. In fact, tensile stresses that follow the peak stress can be even greater outside the interference zone than within it. Primarily, this results from the acceleration of material by the shock and rarefaction waves. Material behind the shock wave has been accelerated outward from the point of impact, forcing it to occupy a greater volume as it moves radially outwards. This causes transverse stresses behind the shock front to become tensile.

The tensile stresses in the interference zone and behind the shock front ultimately lead to tensile failure and fracturing in the target rocks. As the strength of rocks is much lower in tension than in compression, this region of tensile fracturing tends to extend to far greater distances than the material that experiences compressive failure (Melosh, 1989; Wiggins et al., 2019). A large proportion of fracturing and brecciation during cratering results not from the compression of the shock but due to the tension that occurs after compression. The extent of the zone that experiences tensile stresses is strongly dependent on overburden pressure, that is the pressure produced by the mass of rocks above a location. Thus, the volume that experiences tensile failure is comparatively small for larger craters, where the deep regions of the target are under large confining pressures, and tensile failure is enhanced on low gravity bodies.

Tensile stresses can ultimately result in fragmentation and disruption of target bodies. The criterion for catastrophic disruption is commonly defined as Q*, the kinetic energy per unit of target mass required for only 50% of the target mass to remain. Q* primarily varies as a function of target size, strength, and impact velocity, leading to catastrophic disruption being

most favoured in target objects, such as asteroids, that range from ~0.1–1 km in diameter (Housen and Holsapple, 1990; Stewart and Leinhardt, 2009). Tensile fragmentation and disruption due to impacts has played an important role in shaping the development of the early solar system, and in controlling the generation and delivery of meteoroids throughout the solar system. Further consequences of disruptive impacts include the formation of natural satellites, changing the axial tilt or direction of spin of a planetary body, which may lead to severe climate extremes (see **Section 4.5**).

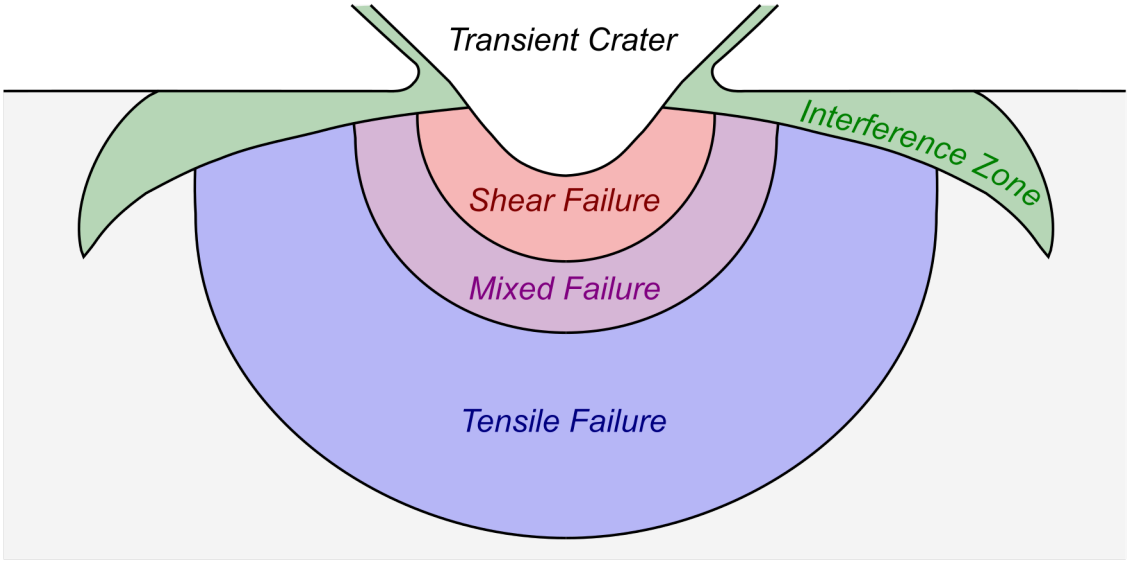

Figure 12: Zones of deformation in the rocks beneath the floor of a growing crater. Close to the point of impact, stresses are strongly compressional and rocks fail in shear. At large distances from the impact point, compressive stresses are low but the material is still accelerated outwards by the expanding shock wave and fails in tension. Between the shear and tensile failure zones is a region of mixed failure mode. Close to the surface, the interaction of the shock wave and rarefaction wave produces the interference zone, a region of the target that experiences tensile stresses (see text for details). Based on Ivanov et al. (1997).

Dilatancy

Dilatancy is the tendency of rocks and granular materials to change volume during shear deformations. From shock passage to the end of crater modification, shear deformation of target rocks is a primary consequence of cratering. The change in porosity caused by dilatancy is a function of the amount of shear strain, the initial porosity, the pressure, and the temperature. Dilatancy is suppressed at high pressures and temperatures, and can produce positive or negative changes in porosity depending on the initial porosity relative to a critically dilatant state of the material. Dilatancy is therefore enhanced in non-porous targets and on low-gravity

bodies where lithostatic pressure gradients are lower. Dilatancy has important effects on the morphology, geophysical signature, and petrophysical properties of impact structures (Collins, 2014). In simple craters, dilatancy contributes to the shallowing of the final crater relative to the transient cavity. Material from the rim of the crater is transported as debris flows into the crater centre. As this occurs, dilatancy acts to bulk out the brecciated rock mass, therefore reducing the final crater depth and making the greatest contribution to the mass deficit of the crater - the mass lost in the crater compared to the pre-impact state. In complex craters, target materials undergo more extreme deformation paths, experiencing dilatancy throughout that path. In these craters, dilatancy in the shocked target rocks makes a greater contribution to the mass deficit of the crater than the impact breccias that may fill the crater. This dilatancy is expressed by fracturing.

Compaction

Impact processes during shock and deformation more generally can also act to reduce the porosity of a material. If a target material has an initially high porosity, shock compression will result in compaction of the material. As this compaction is related to shock compression, it will act prior to any dilatancy or tensile fracturing of the target. Furthermore, shear deformations more generally can act to reduce the porosity of a material by dilatancy if the initial distension is greater than the critical distension of the material.

Uplift

During the early stages of cratering (contact and compression, excavation and the beginning of modification), the target material that will be centrally uplifted are located deep within the planetary interior. As such, they experience limited density reduction prior to uplift. Once uplifted, their lower porosities/higher densities produce a relative mass excess. In addition, mass excesses as a result of central uplift can be greatly aided or even dominated by the effect of density stratification within the target, where most commonly, denser materials are found at greater depths. For example, uplift of the crust-mantle boundary in lunar impact basins is responsible for absolute positive gravity anomalies, so called Mascon basins (Neumann et al., 1996; Melosh et al., 2013).

Hydrothermal Activity

On a longer timescale, and on bodies with abundant volatiles, hydrothermal systems can act to change the overall density of the target. High temperature hydrothermal systems can act to increase porosity by dissolving minerals in the sub-surface. Hydrothermal activity can also act to close pore-spaces through the precipitation of minerals. The overall effect for an extinct impact-related hydrothermal system is generally expected be to be a net closure of pore spaces, and consequent increase of density relative to the original post-modification density.

A Case Example: The Lunar Crust

A notable example how impact processes can lead to large scale density reduction of planetary surfaces can be found on the Moon (**Figures 13 and 14**). The surface of the moon is covered by regolith, a layer of fine-grained, unconsolidated, fragmental debris with little to no cohesion. Regolith forms as a result of comminution and overturn due to small meteorite impacts (Shoemaker et al., 1969). The lunar regolith is ~5 – 20 m thick (Papike et al., 1982; Bart et al., 2011; Yue et al., 2019). Regolith formation is expected on all planetary bodies with thin atmospheres. Beneath the lunar regolith is a layer of rock, 10-25 km thick, that causes extreme scattering of seismic signals (Latham et al., 1972). High resolution gravity data acquired by the Gravity Recovery and Interior Laboratory (GRAIL) spacecraft show that the bulk density of the Lunar Highland crust is 2550 kg m^{-3} (Wieczorek et al., 2013). This suggests, based on remote sensing data and samples, that the lunar crust has an average porosity of ~12% within the top few kilometres of the crust and that porosities typically decrease to ~8 % and ~3-4 % at depths of 10 km and 20 km respectively (Besserer et al., 2014). This layer of highly porous and fragmented rock is known as the "megaregolith" (Hartmann, 1973). The megaregolith is itself composed of an upper and lower layer. The upper megaregolith, sometimes referred to as the "large-scale ejecta layer", is several kilometres thick and is composed of material transported during the formation of large impact craters, either by excavation or collapse (Richardson and Abramov, 2020). The lower megaregolith, sometimes referred to as the "in-situ fragmentation layer", is approximately 10-20 km thick and is the result of bedrock that has been fractured or fragmented by impacts but not ejected or otherwise transported. This fragmentation is predominantly caused by tensile stresses that develop in the wake of impact-induced shock waves (Wiggins et al., 2019).

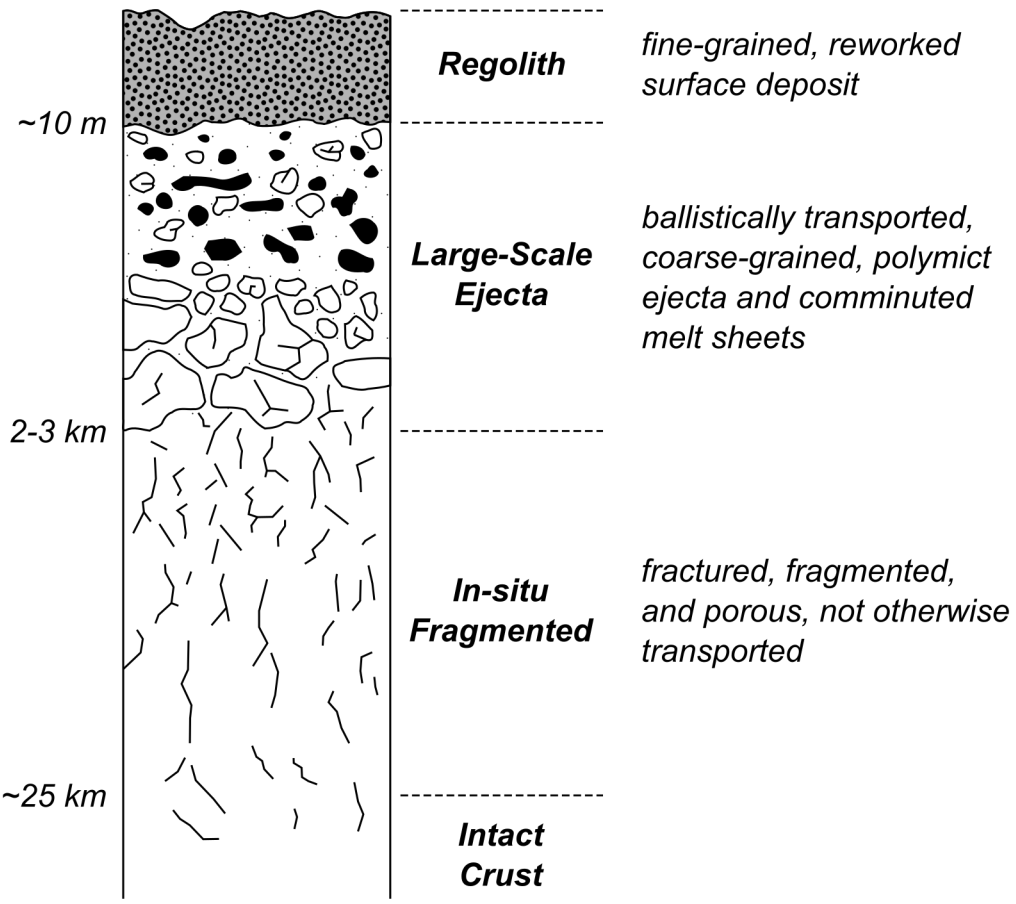

Figure 13: Schematic cross-section of the Lunar upper crust. The upper 5-20 m consists of regolith; loose, unconsolidated fines produced by frequent small impact events. The large-scale ejecta layer beneath is ~2-3 km in thickness. It consists of multiple deposits of impact ejecta from large-scale impact processes. The fragmented layer beneath, ~25 km in thickness, consists of lunar crustal rocks that were fractured in-situ by impact processes. The fragment size increases with depth. Adapted from Hörz et al. (1991).

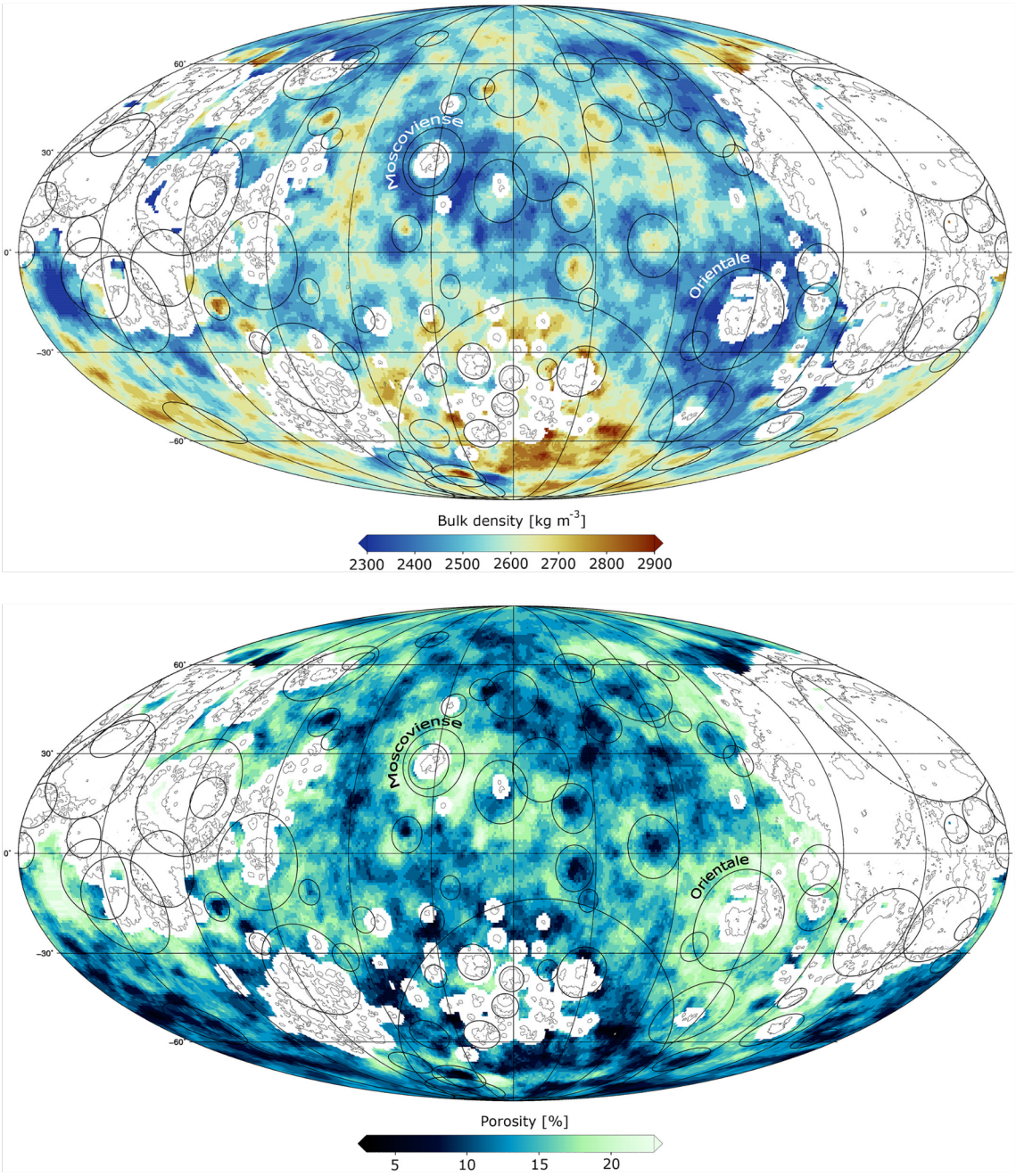

Figure 14: Upper crustal density and porosity maps of the Moon (Wahl et al., 2020). The maps use a Mollweide equal area projection, centred over the lunar farside. Impact basins with diameters >200 km are indicated with black circles, and the lunar mare, which were not analysed for density and porosity, are outlined with thin black lines. Note that each impact basin has a significant effect on the surrounding density and porosity of the lunar crust.

Physical properties of the Target: Thermal Modification

A direct consequence of impacts is the heating, melting, and vaporisation of target materials. The distribution of that heat energy is generally concentrated close to the centre of the impact crater, and close to the surface. Impact heating can have a profound effect on the physical properties of the target material: affecting the magnetic properties of rocks, driving hydrothermal activity, resetting geochronometers, and allowing for the formation of economic deposits.

Magnetism

In general, craters are characterised by magnetic lows, i.e. the process of impact cratering results in demagnetisation of target rocks. Shock is capable of removing natural magnetizations at pressures > 1 GPa (Hargraves and Perkins, 1969; Pohl et al., 1975; Cisowski and Fuller, 1978), and decreasing magnetic susceptibility at pressures > 10 GPa (Kumar and Ward, 1963).

While shock metamorphism is capable of demagnetising target rocks, shock metamorphism can also be one of the causes of short wavelength magnetic anomalies within impact structures. Impacts can induce so-called shock remnant magnetisation (SRM) in the direction of the ambient magnetic field at the time of impact. The intensity of SRM is proportional to the magnitude of the ambient field and decreases with distance from the point of impact (Pohl et al., 1975; Cisowski and Fuller, 1978). SRM most commonly occurs in poorly shocked rocks, at pressures greater than ~ 1 GPa and shock pressures sufficiently low that the material does not exceed the Curie temperatures of the magnetic phases present. Short wavelength anomalies are more generally caused by thermal and/or chemical remnant magnetizations (TRMs and CRMs, respectively). TRMs can be generated as a result of shock melting or by shock heating more generally. Impact melts will often crystallise magnetic carrier phases that generate TRMs in the orientation of the ambient field at the time of crystallisation. At lower post-shock temperatures above the Curie temperature of the magnetic minerals in a given material, remagnetisation of the magnetic carrier phases will also result in TRMs. Partial TRMs can also be generated at post-shock temperatures below the Curie temperature. TRMs can be used as a method of dating impact structures (e.g. Pesonen et al., 1999; Lepaulard et al., 2019). On volatile rich bodies, heating and brecciation of the target in impact craters can result in hydrothermal systems that generate CRMs by the precipitation of magnetic carrier phases. As the timescales of shock, cooling beneath the Curie temperature, and hydrothermal activity are typically orders of magnitude different from each other, it is possible that different

magnetizations within the same impact structure can record different magnetic fields. For example, in the Chicxulub crater, impact melts record a reverse oriented TRM characteristic of polarity chron 29r - the magnetostratigraphic unit at the K-Pg boundary. However, overlying breccia deposits, which were likely deposited below the Curie temperature record both normal and reverse oriented CRMs; normally oriented magnetizations suggest that hydrothermal activity continued at the crater for a minimum of 150 kyr after impact (Kring et al., 2020).

In addition to generating magnetization in target materials, magnetic anomalies can be generated by the redistribution of pre-existing magnetic materials. This is most commonly seen in the formation of long-wavelength magnetic anomalies in large craters which are caused by the uplift of magnetic basement materials.

Geochronometers

While magnetisation in target rocks can be used as a method of dating impact events, isotopic dating is more commonly used. Radiometric dating of impact structures most commonly uses U-Pb or Ar-Ar systematics (Jourdan et al., 2012; Schmieder and Kring, 2020). The most common targets for isotopic dating are impact melt rocks, which may be glassy, or contain mineral fragments whose radioactive clocks were reset, or contain newly crystallised minerals. Additionally, in recent years, advancements of in-situ dating techniques have permitted the combination of micro-structural and geochronological methods whereby impact structures may be dated, even within only partially reset mineral grains (e.g. Darling et al., 2016; Erickson et al., 2017; Timms et al., 2020). Consequently, geochronometers can be applied to date different aspects of the impact cratering process; be it shock metamorphism, post-shock thermal resetting, impact melt crystallisation, and hydrothermal element mobilisation or mineral precipitation (**Figure 15**).

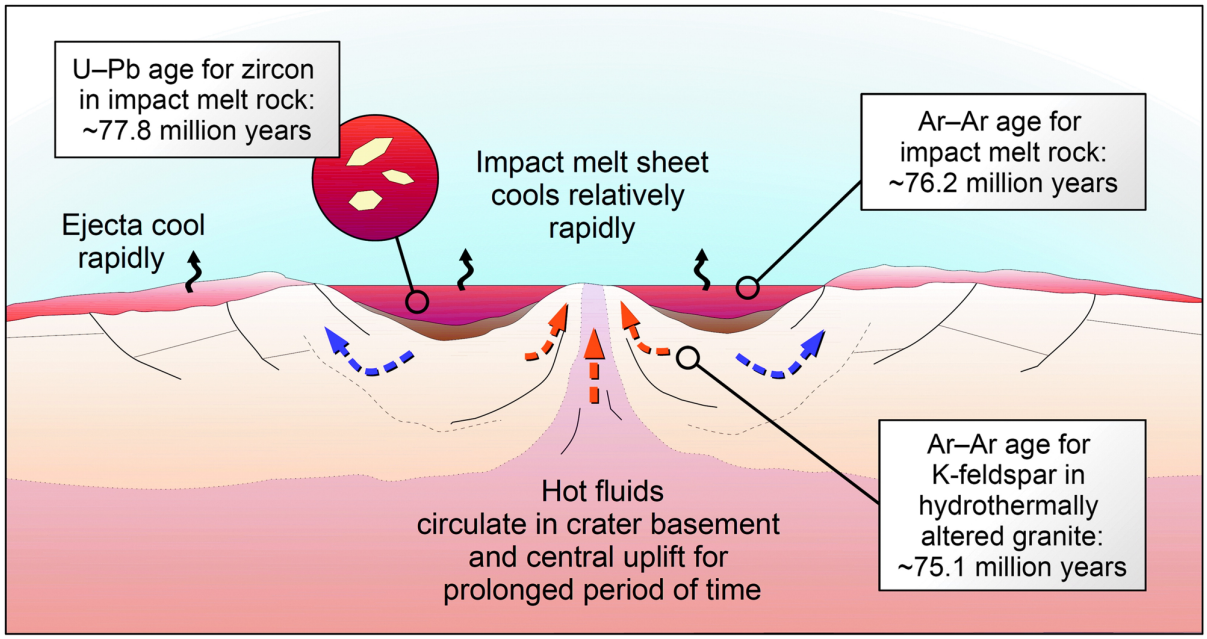

Figure 15: Schematic illustration of geochronological targets within a complex impact structure used to determine impact age and cooling timescale. This diagram shows the ~23 km-diameter Lappajärvi impact structure in Finland with ages from Schmieder and Jourdan (2013) and Kenny et al. (2019). Geochronometers with high closure temperatures (e.g., U-Pb in zircon) record the best-estimate of the impact age, while lower-closure temperature geochronometers (e.g. Ar-Ar in K-feldspar) record prolonged high-temperatures in the crater as a result of hydrothermal activity. Figure from Schmieder and Kring (2020).

Economic Deposits

Impact structures can be important sources of economic deposits. Economic deposits are characterised as pro-, syn-, or epi-genetic (**Table 4**; Grieve, 2005). Progenetic deposits result from the displacement of pre-existing economic deposits, e.g. the uplift of U-bearing lithologies at the Carswell impact structure. Syngenetic deposits can result directly from shock metamorphism, e.g. the production of impact diamonds at Popigai, or the crystallisation of ore minerals in impact melts or hydrothermal systems, e.g. the deposition of Cu-Ni-PGE ores at Sudbury. Epigenetic deposits result from the concentration of economic deposits within impact craters or impactites after the time of impact, e.g. hydrocarbon reservoirs in the Campeche bank related to the Chicxulub impact. All of these types of deposits occur as a consequence of the changes in the location and/or properties of target materials.

Table 4: Genetic groups of natural resource deposits at terrestrial impact structures. From Grieve (2005).

Genetic group	Principal mode of origin	Types of known deposits

Progenetic	Brecciation	Building stone, silica
	Structural displacement	Fe, U, Au
Syngenetic	Phase transitions	Impact diamond
	Crustal melting	Cu, Ni, PGEs, glass
	Hydrothermal activity	Pb, Zn, U, pyrite, Au, zeolite, agate
Epigenetic	Sedimentation	Placer diamond and tektites
	Chemical and biochemical sedimentation	Zeolite, bentonite, evaporites, oil shale, diatomite, lignite, amber, calcium phosphate
	Fluid flow	Oil, natural gas, fresh and mineralised water

Geophysical Signatures of Impact Craters

In this final section, we summarise the geophysical characteristics of impact craters. These characteristics of impact structures are ultimately the result of the changes in physical properties caused by shock, impact, and post-impact processes as described in the previous section.

Gravity Anomalies

Gravity data are sensitive to changes in density within the sub-surface; positive and negative anomalies correspond to higher and lower densities (relative to the surroundings) respectively. The wavelength of a gravity anomaly caused by a sub-surface mass difference, whether low or high mass, increases as its depth increases. Long-wavelength anomalies therefore correspond to deep structures while short-wavelength anomalies correspond to shallow structures. Impact structures are generally associated with long-wavelength negative gravity anomalies, indicating that, on average, cratering acts to reduce the density of the target relative to its pre-impact state. Gravity anomalies associated with craters are typically circular in shape and, in relatively pristine craters, extend to, or slightly beyond, the topographic crater rim. In large craters (on Earth, > ~30 km), gravity anomalies have an annular gravity low that surrounds a relative central high (**Figure 16**). Heavily eroded craters may only have a central gravity high, without an annular low (e.g. Upheaval Dome or Kentland). The magnitude of the negative gravity anomaly of a crater generally increases with crater size up to a limiting value (on Earth, ~30 mGal). This trend of increasing maximum gravity anomaly associated with craters is primarily a result of dilatancy. In small craters, as the size of the impact increases so too does the extent of dilated and fractured rock mass both laterally and vertically. The increasing vertical extent of dilated rocks results in an increase in the maximum gravity anomaly as crater size increases. However, beyond a critical size specific to the gravity of the planetary body and the density of the target, the zone of dilated material cannot extend to greater depths due to pressure supressing dilatancy. Consequently, beyond this critical size, the maximum gravity anomaly remains relatively constant with increasing crater size. On Earth, the transition occurs at approximately 20-30 km diameter (**Figure 17**)

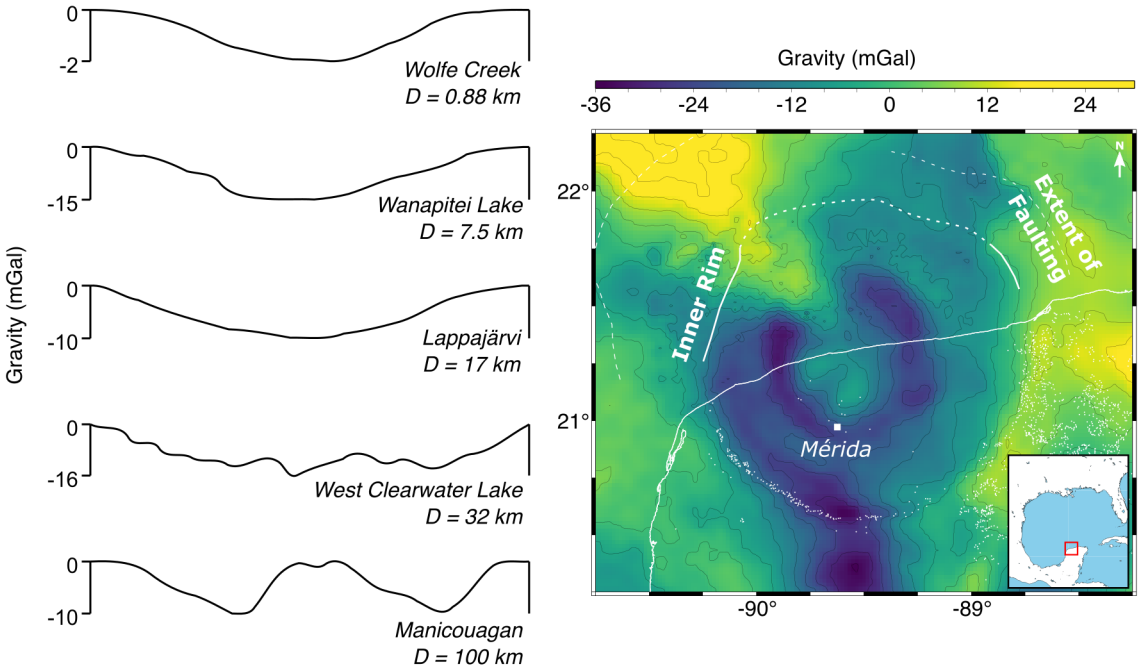

Figure 16: Gravity anomalies of terrestrial impact structures. Gravity profiles from Pilkington and Grieve (1996). Bouguer gravity anomaly map of the Chicxulub impact structure, adapted from Gulick et al. (2013) and refs. therein.

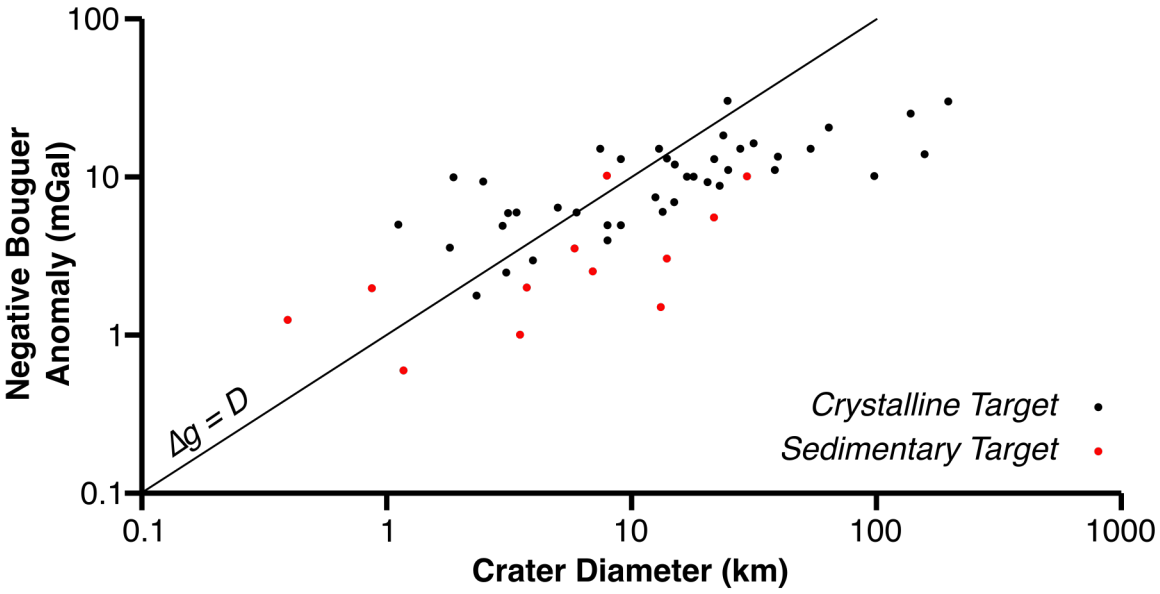

Figure 17: Negative Bouguer gravity anomaly magnitude as a function of crater diameter for terrestrial impact structures. The line $\Delta g = D$ illustrates the proportional relationship between

crater diameter and gravity anomaly magnitude in craters where D < 30 km. Adapted from Pilkington and Grieve (1996).

Magnetic Anomalies

Most studies of the influence of impacts on the magnetic properties of rocks come from studies of the Earth, where magnetic anomalies can be detected as a result of the interaction of magnetic materials in the subsurface with the Earth's magnetic field. The magnitude and shape of a magnetic anomaly for a given body depends upon its location relative to the Earth's magnetic field, thus subsurface modelling of magnetic anomalies is considerably more challenging than subsurface modelling of gravity data. Nevertheless, like gravity data, the wavelength of a magnetic anomaly is related to the depth of the magnetic material in the subsurface. Impact craters on Earth are typically characterised by a magnetic low (e.g. Clark, 1983), a product of demagnetization due to shock (**Section 4.3.4.1**). Large craters may possess short wavelength magnetic anomalies near their centres, related to the precipitation of magnetic minerals in impact melts or hydrothermal systems, and long wavelength magnetic anomalies, related to the uplift of magnetic materials from depth (e.g. Chicxulub, Ortiz-Alemán and Urrutia-Fucugauchi, 2010; **Figure 18**; **Section 4.3.4.1**).

Portions of planetary crusts can be anomalously magnetized due to impacts. The lunar crust is locally magnetized, despite its current lack of a magnetic field, and the weak magnetism of lunar rocks. One particularly large grouping of magnetic anomalies is located on the northern rim of the South Pole–Aitken basin and has been suggested to be caused by deposition of the projectile from the SPA basin impact (Wieczorek et al., 2012), or from the cooling of a large body of impact melt within an ancient lunar magnetic field. Similarly, magnetic anomalies associated with impact structures on Mars have been used to constrain the timing of activity of Mars' now extinct dynamo (Hood et al., 2003; Lillis et al., 2013).

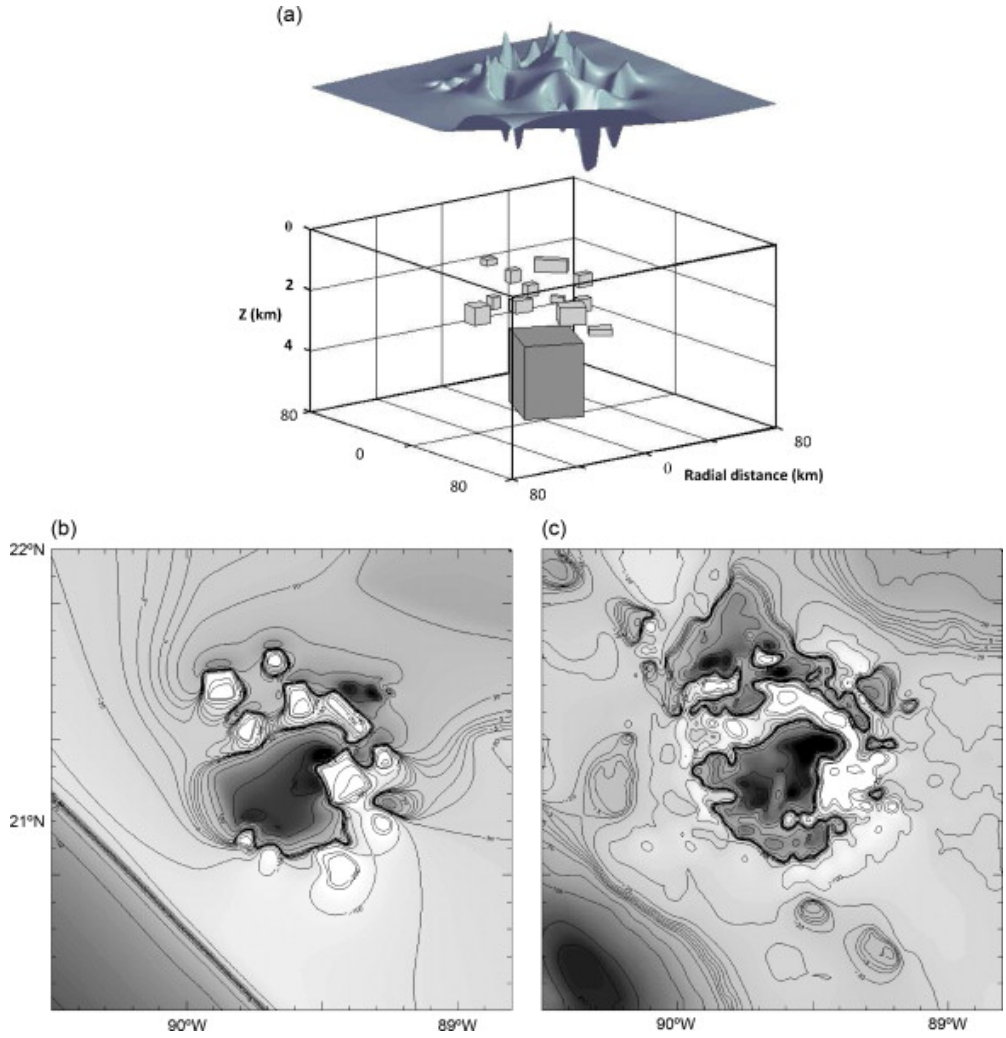

Figure 18: Three-dimensional forward modelling of magnetic anomalies at the Chicxulub Crater. a) three-dimensional configuration of modelled magnetic bodies. b) Synthetic anomaly computed from a). c) Observed anomaly. Figure from Ortiz-Alemán and Urrutia-Fucugauchi (2010).

Compositional Anomalies

Impact craters expose, eject, and exhume rocks that would otherwise remain in the subsurface of tectonically inactive bodies, creating "anomalies" in surface composition as seen from orbit. The 'reach' of this prospecting tool depends upon the depth to the compositionally distinct material (larger craters excavate deeper material). Layering has been observed in the walls of craters of various sizes on numerous bodies throughout the solar system, wherever the resolution is available. Such wall exposures have been used to investigate lunar mare and Martian lava flow thicknesses, and sub-surface composition, etc. (e.g., Kumaresan et al., 2020). In complex craters, the crater formation process also exhumes deep material during central

uplift formation, which can be used to investigate the deeper sub-surface strata of remote planetary bodies (e.g., Ding et al., 2015; Quantin et al., 2012). The exposures of bedrock in the walls and central uplifts of craters can be studied from orbit until erosion or subsequent deposition masks their signatures. Furthermore, compositional differences between ejecta and surrounding target materials can clearly be seen in compositional maps (Mustard et al., 2012, **Figure 19**) of planetary surfaces. However, the relatively rapid erosion of these deposits, even on airless bodies, tends to remove these compositional anomalies for all but the freshest impact craters.

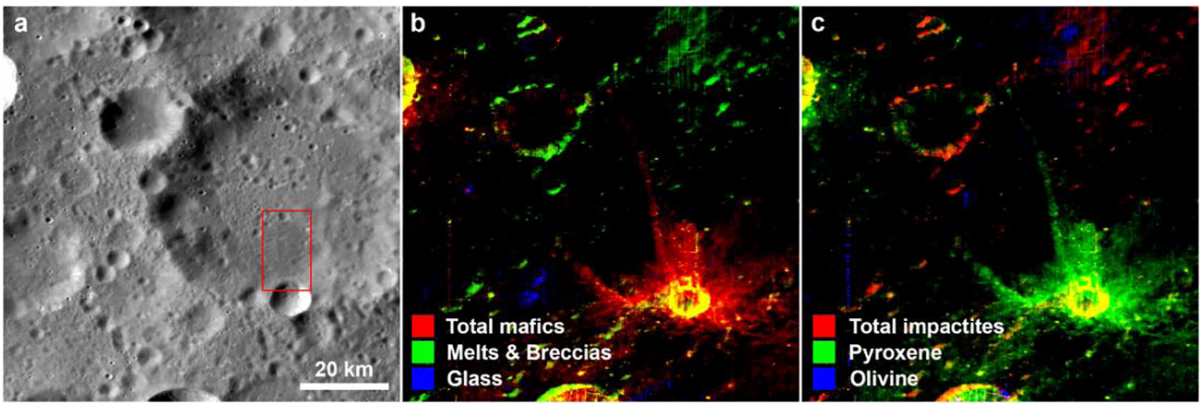

Figure 19: Example of a compositionally distinct impact ejecta deposit on the Moon. This example is shown in a) visual wavelengths by LROC WAC and in two visualizations from Chandrayan's Moon Mineralogy Mapper (M3): b) Red represents the combined mafic material (pyroxenes and olivines), green represents impact melt and breccia, and blue represents quenched glass. (c) Spectral unmixing results, where red represents the combined impactite deposits (quenched glass, impact melts and breccias), green represents pyroxene-rich material and blue represents olivine-rich material. Figure from Neish et al., 2021.

Seismic Properties

Impact cratering can have a profound effect on the seismic properties of the target; that is, the velocity, impedance, and attenuation of seismic waves. These changes are due to a general increase in porosity, fracturing, and brecciation that lead to reduced seismic velocities, higher attenuation, and decreased coherent reflectivity in the target rocks. A number of exceptions to these general trends occur, such as in centrally uplifted regions or in solidified impact melts where seismic velocities and reflectivity can be high (Morgan and Rebolledo-Vieyra, 2012).

Electrical Properties

The electrical resistivity of geological materials is generally very high. In the presence of conductive fluids, resistivity decreases. Therefore, on bodies such as Earth where pore spaces in the subsurface are generally filled with saline water, resistivity generally decreases with increasing porosity, fracturing, and brecciation. The electrical properties of rocks are usually determined by direct resistivity or magnetotelluric surveying. Impact craters are generally characterised by low resistivities.

Table 5: Geophysical anomalies associated with impact craters. Table from Morgan and Rebolledo-Vieyra (2012).

Method	Physical Properties	Resolution[a]	Signature[b]	
Gravity	Density	Low (undefined)	Gravity low (negative)	Impact fracturing, basin infill, impact breccias, peak ring
	Mass excess/deficit		Central high (D > 30 km)	Central uplift
Magnetics	Magnetic Susceptibility	Low (undefined)	Magnetic low (D < 40 km)	Demagnetized target rocks
	Remnant Magnetism		Short λ anomalies (D > 10 km)	Shock metamorphism, hydrothermal processes, thermoremnent magnetization (TRM)
			Long λ anomaly (D > 40 km)	Central uplift
Direct Resistivity	Resistivity	Low (undefined)	Low resistivity	Impact breccias, basin infill, fractured rocks, peak ring
			High resistivity	Central uplift, impact melts
Magnetotelluric	Resistivity	Medium (~skin depth)	Low resistivity	Impact breccias, basin infill, fractured rocks, peak ring
			High resistivity	Central uplift, impact melts
Seismic Refraction	Velocity	Medium-high (Fresnel Zone)	Low velocity	Impact breccias, basin infill, fractured rock, peak ring
			High velocity	Central uplift, impact melts
Seismic Reflection	Acoustic impedance	High (~wavelength)	Reflectivity	Target rocks, megablock zone, faulting, crater rim, basin infill, central peak, peak ring, central uplift, melt sheet, max. depth of disruption
			Loss of coherent reflectivity	Impact breccias, fractured/brecciated rocks
Ground-penetrating radar	Electric and Magnetic properties	High (~wavelength)	Reflectivity	Crater floor (small craters)

[a]The dimensions of the smallest body that can be resolved with each geophysical method are shown in parentheses. Resolution can also be adversely affected by survey design, noise, and modelling approach adopted.

[b]D is crater diameter. A magnetic low means that there is only a small magnetic anomaly (positive or negative), whereas a gravity low means that the gravity anomaly is negative.

Global Consequences of Impacts and Implications for Future Geologic Processes

In addition to the impact effects listed so far, large impacts can also indirectly affect target geology on global scales. This short section explores the global outcomes of large impacts, beginning with the multi-ring basin size range, and working upwards towards catastrophic disruption of the target body.

Fundamentally, crater formation moves a section of the target away from its equilibrium state of a flat plain. The excavation of material during impact crater formation, combined with the lower density of the fragmented sub-crater debris relative to the surrounding area, creates an isostatically uncompensated feature. This produces a circular 'gravity low' anomaly which has aided the identification of some terrestrial impact structures, (e.g. Chicxulub; Hildebrand et al., 1991) and sites of ancient impact basins on the Moon (Evans et al., 2016) .

The forces present after crater formation act to isostatically compensate for the loss of material and density reduction. Over time, the crater floor will rise in response to these forces and the rims become subdued, moving the crater topography towards isostatic equilibrium. The mass movement of solid material is known as "viscous relaxation". All materials flow under applied stress over long enough time scales. The rate of viscous flow is temperature, strain rate and crater-size dependent and can be imperceptibly slow at low temperatures and for small craters. **Figure 20a** displays the Memphis Facula "palimpsest" on the Galilean moon Ganymede, highlighting its flattened high-albedo inner section remaining after the viscous relaxation of this large impact crater. A potential in-progress palimpsest – the penepalimpsest Buto Facula - is also images in Figure 20a. Buto still retains some topography that hints at an initial crater-form like that of anomalous dome and/or central pit crater, prior to viscous relaxation softening its topography.

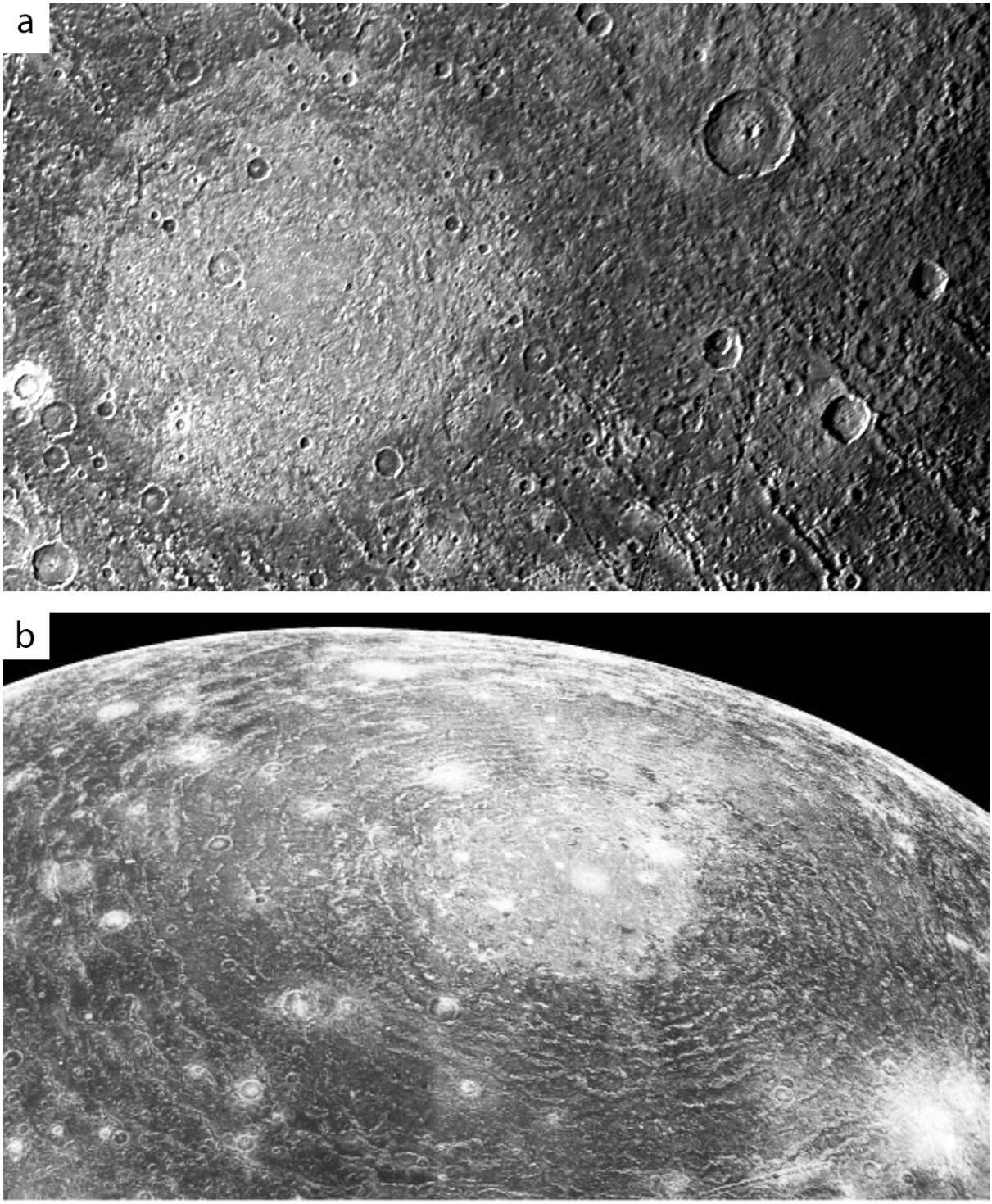

Figure 20: a) Galileo image of the Memphis Facula palimpsest (left) and Buto Facula pene-palimpsest (top right) on Jupiter's icy moon Ganymede. Memphis Facula is approximately 340 km across. b) Voyager 1 image of the Valhalla multi-ring impact basin on Jupiter's moon Callisto. The bright central region is approximately 360 km across and has very little relief after viscous relaxation of the original crater structure. The far-reaching ring system around the impact point covers an entire hemisphere of Callisto.

The far-reaching concentric rings of multi-ring basins such as Valhalla can span across whole hemispheres of the target body and potentially extend down to the base of the brittle lithosphere (McKinnon and Melosh, 1980). Deep fractures, impact-generated or not, provide conduits for surface-to-subsurface material exchange (Geissler et al., 1998). As well as having implications for astrobiology, the presence of global impact-related fractures influences planetary geology by potentially producing sites for later magmatism or cryomagmatism (e.g. Steinbrügge et al., 2020 and references therein). In the case of Valhalla and Ganymede's Galileo Regio trough system, the extensive fracturing is thought to be formed, not as a direct result of the impact energy rippling through the crust, but due to the crustal response to the presence of a mass deficit: The liquid mantle flowed to fill the gap left by the impact, fracturing the more brittle ice of the upper crust in a concentric pattern (McKinnon and Melosh, 1980).

The mass deficit produced by the presence of a large impact basin can be large enough to perturb the target body relative to its spin axis (Gold, 1955; Nimmo and Matsuyama, 2007). This is also true for impact basins where significant mantle upwelling or basin infill has occurred, producing a mass concentration (e.g. Sputnik Basin's nitrogen ice fill; Johnson et al., 2021). In the case of icy moons, with a crust decoupled from their silicate interiors by sub-surface oceans, this can result in true polar wander as the ice crust reorients to place the mass anomaly at a more energy-efficient location – Mass deficits at the poles, and mass concentrations at the equator (Melosh, 1975). This has the result of moving previously equatorial terrains into polar positions (and vice versa), radically changing the geological processes that are ongoing over that portion of crust, and thus changing the geology of the target.

Some impacts, occurring at fortuitous velocities and angles, are large enough to reorient the spin axis itself (e.g. Kegerreis et al., 2018 and references therein), or even the spin direction (Davies 2008). Impacts of the size necessary for such fundamental alteration are likely to have removed a large portion of the planetary atmosphere and/or ocean (if the body had one). The removal of any amount of volatiles will affect weather systems, surface conditions, and the geologic processes occurring on that body. The types of rocks formed at the surface of that body from then on will have been fundamentally changed. If a spin-axis change resulted in a large spin-axis obliquity, the planetary body's future now includes more extreme seasons as the polar regions increase in size. In the case of Pluto, the temperature difference between the fully illuminated north pole to the constantly dark south pole during the northern summer, causes extreme volatile cycling. This drives sublimation and erosion of the surface ices, that is far more active than would be expected were Pluto's spin axis less oblique (Binzel et al., 2017).

The largest impacts can disrupt a planetary body, partially or "catastrophically". The size of impactor required to cause catastrophic disruption, defined as an impact event that produces a largest fragment that is half the size of the original target, varies for target body gravity and material strength (Benz and Asphaug, 1999). A famous example of a giant planetary collision is the Moon-forming impact where a Mars-sized projectile struck the early Earth to produce the Earth-Moon system (e.g. Asphaug et al., 2021 and references therein). Although damaging the Earth in the short term, the presence of a large satellite has stabilized the Earth's spin axis, constraining our axial 'wobble' to a modest 2.4 degrees over the last million years, compared to Mars 20.6 degree variances (Ward et al., 1992). A stable spin axis maintains a consistency to the climate zones (polar, equatorial, etc) that may have allowed for life on Earth to have developed undisrupted by severe fluctuations in environmental conditions. In addition, the presence of the Moon produces inter-tidal environments that may have assisted the progression of life out of the seas and onto land.

Although the current day geology of our solar system is far removed, temporally, from the devastating impact event(s) which changed axis obliquity, rotation direction, formed new moons, etc., each planetary body's geology is ultimately the indirect result of a series of impacts, each creating a unique set of environmental conditions that produced the geology we see today.

Summary

Impacts have a profound influence on target materials and their properties. The passage of a shock wave can lead to vaporisation, melting, solid-state shock metamorphism, and fracturing and fragmentation of the target. Subsequently, material can be transported and deformed by the processes of crater excavation and modification. The materials in the final crater are generally less dense and some properties, such as magnetism, may be reset as a consequence of their impact-related thermodynamic and deformation paths. The net effect of multiple impacts can have important consequences for the development of planetary surfaces. In this chapter, we have primarily focussed on the specific consequences of impacts on target geology at the site of impact. However, impacts can affect the geology of target bodies in less direct but still important ways, for example: disruption and accretion of planetesimals, planetary supply of volatiles, magma ocean formation, and moon-forming impacts.

References

Ahrens, T.J., O'Keefe, J.D., 1987. Impact on the earth, ocean and atmosphere. International Journal of Impact Engineering, Hypervelocity Impact Proceedings of the 1986 Symposium 5, 13–32. https://doi.org/10.1016/0734-743X(87)90028-5

Ahrens, T.J., O'Keefe, J.D., 1977. Equations of state and impact-induced shock-wave attenuation on the moon, in: Impact and explosion cratering: Planetary and terrestrial implications. New York, Pergamon Press, Inc., p. 639-656.

Ahrens, T.J., O'Keefe, J.D., 1972. Shock melting and vaporization of lunar rocks and minerals. *The Moon*, *4*, 214-249.

Asphaug, E., Emsenhuber, A., Cambioni, S., Gabriel, T.S. and Schwartz, S.R., 2021. Collision chains among the terrestrial planets. III. Formation of the Moon. *The planetary science journal*, *2*(5), p.200.

Baratoux, D., & Melosh, H. J. (2003). The formation of shatter cones by shock wave interference during impacting. *Earth and Planetary Science Letters*, *216*(1-2), 43-54.

Bart, G.D., Nickerson, R.D., Lawder, M.T., Melosh, H.J., 2011. Global survey of lunar regolith depths from LROC images. Icarus 215, 485–490. https://doi.org/10.1016/j.icarus.2011.07.017

Benz, W. and Asphaug, E., 1999. Catastrophic disruptions revisited. *Icarus*, *142*(1), pp.5-20.

Besserer, J., Nimmo, F., Wieczorek, M.A., Weber, R.C., Kiefer, W.S., McGovern, P.J., Andrews-Hanna, J.C., Smith, D.E., Zuber, M.T., 2014. GRAIL gravity constraints on the vertical and lateral density structure of the lunar crust. Geophysical Research Letters 41, 5771–5777. https://doi.org/10.1002/2014GL060240

Binzel, R.P., Earle, A.M., Buie, M.W., Young, L.A., Stern, S.A., Olkin, C.B., Ennico, K., Moore, J.M., Grundy, W., Weaver, H.A. and Lisse, C.M., 2017. Climate zones on Pluto and Charon. *Icarus*, *287*, pp.30-36.

Cavosie, A.J., Timms, N.E., Ferrière, L., Rochette, P. (2018). FRIGN zircon—The only terrestrial mineral diagnostic of high-pressure and high-temperature shock deformation. *Geology*, *46*(10), 891-894.

Christeson, G.L., Collins, G.S., Morgan, J.V., Gulick, S.P., Barton, P.J., Warner, M.R., 2009. Mantle deformation beneath the Chicxulub impact crater. *Earth and Planetary Science Letters*, *284*(1-2), 249-257.

Christian, J.W., Mahajan, S. (1995). Deformation twinning. *Progress in materials science*, *39*(1-2), 1-157.

Cintala, M.J., Grieve, R.A.F., 1998. Scaling impact melting and crater dimensions: Implications for the lunar cratering record. *Meteoritics & Planetary Science*, *33*(4), 889-912.

Cisowski, S.M., Fuller, M., 1978. The effect of shock on the magnetism of terrestrial rocks. Journal of Geophysical Research: Solid Earth 83, 3441–3458. https://doi.org/10.1029/JB083iB07p03441

Clark, J. F. (1983). *Magnetic survey data at meteoritic impact sites in North America*. Geomagnetic Service of Canada.

Collins, G. S. (2014). Numerical simulations of impact crater formation with dilatancy. *Journal of Geophysical Research: Planets*, *119*(12), 2600-2619.

Dahl, J.M., Schultz, P.H., 2001. Measurement of stress wave asymmetries in hypervelocity projectile impact experiments. International Journal of Impact Engineering 26, 145–155. https://doi.org/10.1016/S0734-743X(01)00077-X

Darling, J.R., Moser, D.E., Barker, I.R., Tait, K.T., Chamberlain, K.R., Schmitt, A.K., Hyde, B.C., 2016. Variable microstructural response of baddeleyite to shock metamorphism in young basaltic shergottite NWA 5298 and improved U–Pb dating of Solar System events. Earth and Planetary Science Letters 444, 1–12. https://doi.org/10.1016/j.epsl.2016.03.032

Davies, E. J., Carter, P. J., Root, S., Kraus, R. G., Spaulding, D. K., Stewart, S. T., & Jacobsen, S. B., 2020. Silicate melting and vaporization during rocky planet formation. *Journal of Geophysical Research: Planets*, *125*(2), e2019JE006227.

Davies, J.H., 2008. Did a mega-collision dry Venus' interior?. *Earth and Planetary Science Letters*, *268*(3-4), pp.376-383.

Dietz, R. S., & Butler, L. W. (1964). Shatter-cone orientation at Sudbury, Canada. *Nature*, *204*, 280-281.

Ding, N., Bray, V.J., McEwen, A.S., Mattson, S.S., Okubo, C.H., Chojnacki, M., Tornabene, L.L., 2015. The central uplift of Ritchey crater, Mars. Icarus 252, 255–270. https://doi.org/10.1016/j.icarus.2014.11.001

Erickson, T.M., Timms, N.E., Kirkland, C.L., Tohver, E., Cavosie, A.J., Pearce, M.A., Reddy, S.M., 2017. Shocked monazite chronometry: integrating microstructural and in situ isotopic age data for determining precise impact ages. Contributions to Mineralogy and Petrology 172, 11. https://doi.org/10.1007/s00410-017-1328-2

Evans, A.J., Soderblom, J.M., Andrews-Hanna, J.C., Solomon, S.C., Zuber, M.T., 2016. Identification of buried lunar impact craters from GRAIL data and implications for the nearside maria. Geophysical Research Letters 43, 2445–2455. https://doi.org/10.1002/2015GL067394

French, B.M., Koeberl, C., 2010. The convincing identification of terrestrial meteorite impact structures: What works, what doesn't, and why. Earth-Science Reviews 98, 123–170. https://doi.org/10.1016/j.earscirev.2009.10.009

Geissler, P. E., Greenberg, R., Hoppa, G., McEwen, A., Tufts, R., Phillips, C., Clark, B., Ockert-Bell, M., Helfenstein, P., Burns, J., Veverka, J., Sullivan, R., Greeley, R., Pappalar, R.T., Head, J.W., Belton, M.J.S., Denk, T. (1998). Evolution of lineaments on Europa: Clues from Galileo multispectral imaging observations. *Icarus*, *135*(1), 107-126.

Grieve, R.A.F., 2005. Economic natural resource deposits at terrestrial impact structures. Geological Society, London, Special Publications 248, 1–29. https://doi.org/10.1144/GSL.SP.2005.248.01.01

Grieve, R.A.F., 1987. Terrestrial Impact Structures. Annual Review of Earth and Planetary Sciences 15, 245–270. https://doi.org/10.1146/annurev.ea.15.050187.001333

Grieve, R.A.F., Langenhorst, F., Stöffler, D., 1996. Shock metamorphism of quartz in nature and experiment: II. Significance in geoscience*. Meteoritics & Planetary Science 31, 6–35. https://doi.org/10.1111/j.1945-5100.1996.tb02049.x

Grieve, R.A.F., Cintala, M.J. (1992). An analysis of differential impact melt-crater scaling and implications for the terrestrial impact record. *Meteoritics*, *27*(5), 526-538.

Gold, T., 1955. Instability of the Earth's axis of rotation. *Nature*, *175*, pp.526-529.

Gulick, S.P.S., Christeson, G.L., Barton, P.J., Grieve, R.A.F., Morgan, J.V., Urrutia-Fucugauchi, J., 2013. Geophysical Characterization of the Chicxulub Impact Crater. Reviews of Geophysics 51, 31–52. https://doi.org/10.1002/rog.20007

Hargraves, R.B., Perkins, W.E., 1969. Investigations of the effect of shock on natural remanent magnetism. Journal of Geophysical Research (1896-1977) 74, 2576–2589. https://doi.org/10.1029/JB074i010p02576

Hartmann, W.K., 1973. Ancient lunar mega-regolith and subsurface structure. Icarus 18, 634–636. https://doi.org/10.1016/0019-1035(73)90066-3

Hildebrand, A.R., Penfield, G.T., Kring, D.A., Pilkington, M., Z, A.C., Jacobsen, S.B., Boynton, W.V., 1991. Chicxulub Crater: A possible Cretaceous/Tertiary boundary impact crater on the Yucatán Peninsula, Mexico. Geology 19, 867–871. https://doi.org/10.1130/0091-7613(1991)019<0867:CCAPCT>2.3.CO;2

Hood, L.L., Richmond, N.C., Pierazzo, E., Rochette, P., 2003. Distribution of crustal magnetic fields on Mars: Shock effects of basin-forming impacts. Geophysical Research Letters 30. https://doi.org/10.1029/2002GL016657

Hörz, F., G. Grieve, G. Heiken, P. Spudis, and A. Binder (1991), Lunar surface processes, in *The Lunar Sourcebook*, edited by G. Heiken, D. T. Vaniman, and B. M. French, pp. 61–111, Cambridge Univ. Press, New York.

Housen, K.R., Holsapple, K.A., 1990. On the fragmentation of asteroids and planetary satellites. Icarus 84, 226–253. https://doi.org/10.1016/0019-1035(90)90168-9

Ivanov, B.A., Deniem, D., Neukum, G. (1997). Implementation of dynamic strength models into 2D hydrocodes: Applications for atmospheric breakup and impact cratering. *International Journal of Impact Engineering*, *20*(1-5), 411-430.

Johnson, P.E., Keane, J.T., Young, L.A. and Matsuyama, I., 2021. New Constraints on Pluto's Sputnik Planitia Ice Sheet from a Coupled Reorientation–Climate Model. *The Planetary Science Journal*, *2*(5), p.194.

Jourdan, F., Reimold, W.U., Deutsch, A., 2012. Dating Terrestrial Impact Structures. Elements 8, 49–53. https://doi.org/10.2113/gselements.8.1.49

Kegerreis, J.A., Teodoro, L.F.A., Eke, V.R., Massey, R.J., Catling, D.C., Fryer, C.L., Korycansky, D.G., Warren, M.S. and Zahnle, K.J., 2018. Consequences of giant impacts on early Uranus for rotation, internal structure, debris, and atmospheric erosion. *The Astrophysical Journal*, *861*(1), p.52.

Kenkmann, T., Poelchau, M.H., Wulf, G., 2014. Structural geology of impact craters. Journal of Structural Geology 62, 156–182. https://doi.org/10.1016/j.jsg.2014.01.015

Kenny, G.G., Schmieder, M., Whitehouse, M.J., Nemchin, A.A., Morales, L.F., Buchner, E., Bellucci, J.J., Snape, J. F., 2019. A new U-Pb age for shock-recrystallised zircon from the Lappajärvi impact crater, Finland, and implications for the accurate dating of impact events. *Geochimica et Cosmochimica Acta*, *245*, 479-494.

Kowitz, A., Güldemeister, N., Reimold, W.U., Schmitt, R.T., Wünnemann, K., 2013. Diaplectic quartz glass and SiO2 melt experimentally generated at only 5 GPa shock pressure in porous sandstone: Laboratory observations and meso-scale numerical modeling. Earth and Planetary Science Letters 384, 17–26. https://doi.org/10.1016/j.epsl.2013.09.021

Kowitz, A., Güldemeister, N., Schmitt, R.T., Reimold, W.-U., Wünnemann, K., Holzwarth, A., 2016. Revision and recalibration of existing shock classifications for quartzose rocks using low-shock pressure (2.5–20 GPa) recovery experiments and mesoscale numerical modeling. Meteoritics & Planetary Science 51, 1741–1761. https://doi.org/10.1111/maps.12712

Kraus, R.G., Stewart, S.T., Swift, D.C., Bolme, C.A., Smith, R.F., Hamel, S., Spaulding, D.K., Hicks, D.G., Eggert, J.H., Collins, G.W., 2012. Shock vaporization of silica and the thermodynamics of planetary impact events. *Journal of Geophysical Research: Planets*, *117*(E9).

Kraus, R.G., Senft, L.E., & Stewart, S.T. (2011). Impacts onto H2O ice: Scaling laws for melting, vaporization, excavation, and final crater size. *Icarus*, *214*(2), 724-738.

Kring, D.A., Tikoo, S.M., Schmieder, M., Riller, U., Rebolledo-Vieyra, M., Simpson, S.L., Osinski, G.R., Gattacceca, J., Wittmann, A., Verhagen, C.M., Cockell, C.S., Coolen, M.J.L., Longstaffe, F.J., Gulick, S.P.S., Morgan, J.V., Bralower, T.J., Chenot, E., Christeson, G.L., Claeys, P., Ferrière, L., Gebhardt, C., Goto, K., Green, S.L., Jones, H., Lofi, J., Lowery, C.M., Ocampo-Torres, R., Perez-Cruz, L., Pickersgill, A.E., Poelchau, M.H., Rae, A.S.P., Rasmussen, C., Sato, H., Smit, J., Tomioka, N., Urrutia-Fucugauchi, J., Whalen, M.T., Xiao, L., Yamaguchi, K.E., 2020. Probing the hydrothermal system of the Chicxulub impact crater. Science Advances 6, eaaz3053. https://doi.org/10.1126/sciadv.aaz3053

Krüger, T., Kenkmann, T., Hergarten, S., 2017. Structural uplift and ejecta thickness of lunar mare craters: New insights into the formation of complex crater rims. Meteoritics & Planetary Science 52, 2220–2240. https://doi.org/10.1111/maps.12925

Kumar, A., Ward, S.H., 1963. The Effect of Explosive Shock on the Susceptibility of Magnetite Grout Mixture (No. UCRL-13088; MT-63-10). California. Univ., Berkeley. Inst. of Engineering Research.

Kumaresan, P.R., Saravanavel, J., Palanivel, K., 2020. Lithological mapping of Eratosthenes crater region using Moon Mineralogy Mapper of Chandrayaan-1. Planetary and Space Science 182, 104817. https://doi.org/10.1016/j.pss.2019.104817

Langenhorst, F., & Deutsch, A. (1994). Shock experiments on pre-heated α-and β-quartz: I. Optical and density data. *Earth and Planetary Science Letters*, *125*(1-4), 407-420.

Latham, G.V., Ewing, M., Press, F., Sutton, G., Dorman, J., Nakamura, Y., Toksoz, N., Lammlein, D., Duennebier, F., 1972. Passive seismic experiment.

Lepaulard, C., Gattacceca, J., Swanson-Hysell, N., Quesnel, Y., Demory, F., Osinski, G.R., 2019. A Paleozoic age for the Tunnunik impact structure. Meteoritics & Planetary Science 54, 740–751. https://doi.org/10.1111/maps.13239

Lillis, R.J., Robbins, S., Manga, M., Halekas, J.S., Frey, H.V., 2013. Time history of the Martian dynamo from crater magnetic field analysis. Journal of Geophysical Research: Planets 118, 1488–1511. https://doi.org/10.1002/jgre.20105

Maxwell, D.E., 1977. Simple Z model for cratering, ejection, and the overturned flap, in: Impact and explosion cratering: Planetary and terrestrial implications. New York, Pergamon Press, Inc., p. 1003-1008.

McKinnon, W.B., Melosh, H.J., 1980. Evolution of Planetary Lithospheres: Evidence from Multiringed Structures onf Ganymede and Callisto, Icarus 44:454-471

Melosh, H.J., 1989. Impact cratering: A geologic process. Oxford University Press.

Melosh, H.J., 1975. Large impact craters and the Moon's orientation. *Earth and Planetary Science Letters*, *26*(3), pp.353-360.

Melosh, H.J., Freed, A.M., Johnson, B.C., Blair, D.M., Andrews-Hanna, J.C., Neumann, G.A., Phillips, R.J., Smith, D.E., Solomon, S.C., Wieczorek, M.A., Zuber, M.T., 2013. The Origin of Lunar Mascon Basins. Science 340, 1552–1555. https://doi.org/10.1126/science.1235768

Melosh, H.J., Ivanov, B.A., 1999. Impact Crater Collapse. Annual Review of Earth and Planetary Sciences 27, 385–415. https://doi.org/10.1146/annurev.earth.27.1.385

Milton, D. J., Glikson, A. Y., & Brett, R. (1996). Gosses Bluff-a latest Jurassic impact structure, central Australia. Part 1: geological structure, stratigraphy, and origin. *AGSO Journal of Australian Geology and Geophysics*, *16*(4), 453-486.

Morgan, J., Rebolledo-Vieyra, M., 2012. Geophysical Studies of Impact Craters, in: Impact Cratering. John Wiley & Sons, Ltd, pp. 211–222. https://doi.org/10.1002/9781118447307.ch14

Mustard, J.F., Pieters, C.M., Isaacson, P.J., Head, J.W., Besse, S., Clark, R.N., Klima, R.L., Petro, N.E., Staid, M.I., Sunshine, J.M., Runyon, C.J., Tompkins, S., 2012. Compositional diversity and geologic insights of the Aristarchus crater from Moon Mineralogy Mapper data. Journal of Geophysical Research: Planets: 116(E6): 0148-0227. https://doi.org/10.1029/2010JE003726

Neish, C. D., Cannon, K. M., Tornabene, L. L., Flemming, R. L., Zanetti, M., & Pilles, E. (2021). Spectral properties of lunar impact melt deposits from Moon Mineralogy Mapper (M3) data. *Icarus*, *361*, 114392.

Neumann, G.A., Zuber, M.T., Smith, D.E., Lemoine, F.G., 1996. The lunar crust: Global structure and signature of major basins. Journal of Geophysical Research: Planets 101, 16841–16863. https://doi.org/10.1029/96JE01246

Nimmo, F. and Matsuyama, I., 2007. Reorientation of icy satellites by impact basins. *Geophysical Research Letters*, *34*(19).
Ortiz-Alemán, C., Urrutia-Fucugauchi, J., 2010. Aeromagnetic anomaly modeling of central zone structure and magnetic sources in the Chicxulub crater. Physics of the Earth and Planetary Interiors 179, 127–138. https://doi.org/10.1016/j.pepi.2010.01.007
Osinski, G.R., Ferrière, L. (2016). Shatter cones:(Mis) understood?. *Science Advances*, *2*(8), e1600616.
Papike, J.J., Simon, S.B., Laul, J.C., 1982. The lunar regolith: Chemistry, mineralogy, and petrology. Reviews of Geophysics 20, 761–826. https://doi.org/10.1029/RG020i004p00761
Pesonen, L.J., Elo, S., Lehtinen, M., Jokinen, T., Puranen, R., Kivekäs, L., 1999. Lake Karikkoselkä impact structure, central Finland: New geophysical and petrographic results. https://doi.org/10.1130/0-8137-2339-6.131
Pickersgill, A.E., Jaret, S.J., Pittarello, L., Fritz, J.R. Harris, S., 2021. Shock effects in feldspars: An overview, Large Meteorite Impacts and Planetary Evolution VI.
Pierazzo, E., Melosh, H.J., 2000a. Melt Production in Oblique Impacts. Icarus 145, 252–261. https://doi.org/10.1006/icar.1999.6332
Pierazzo, E., Melosh, H.J., 2000b. Understanding oblique impacts from experiments, observations, and modeling. Annual Review of Earth and Planetary Sciences 28, 141–167. https://doi.org/10.1146/annurev.earth.28.1.141
Pierazzo, E., Vickery, A.M., Melosh, H.J., 1997. A reevaluation of impact melt production. Icarus 127, 408–423. https://doi.org/10.1006/icar.1997.5713
Pierazzo, E., Artemieva, N.A., Ivanov, B.A., 2005, Starting conditions for hydrothermal systems underneath Martian craters: Hydrocode Modeling. *Large meteorite impacts III* 384 (2005): 443-457.
Pilkington, M., Grieve, R.A.F., 1992. The geophysical signature of terrestrial impact craters. *Reviews of Geophysics*, *30*(2), 161-181.
Poelchau, M.H., Kenkmann, T., 2011. Feather features: A low-shock-pressure indicator in quartz. Journal of Geophysical Research: Solid Earth 116. https://doi.org/10.1029/2010JB007803
Pohl, J., Bleil, U., & Bornemann, U. (1975). Shock magnetization and demagnetization of basalt by transient stress up to 10 kbar. *Journal of Geophysics*, *41*(1), 23-41.
Quantin, C., Flahaut, J., Clenet, H., Allemand, P., Thomas, P., 2012. Composition and structures of the subsurface in the vicinity of Valles Marineris as revealed by central uplifts of impact craters. Icarus 221, 436–452. https://doi.org/10.1016/j.icarus.2012.07.031
Richardson, J.E., Abramov, O., 2020. Modeling the Formation of the Lunar Upper Megaregolith Layer. Planet. Sci. J. 1, 2. https://doi.org/10.3847/PSJ/ab7235
Rae, A.S.P., Poelchau, M.H., Kenkmann, T. (2021). Stress and strain during shock metamorphism. *Icarus*, *370*, 114687.
Roddy, D.J., 1977. Large-scale impact and explosion craters: Comparisons of morphological and structural analogs, in: Impact and explosion cratering: Planetary and terrestrial implications. New York, Pergamon Press, Inc., p. 185-246.
Sagy, A., Reches, Z.E., Fineberg, J. (2002). Dynamic fracture by large extraterrestrial impacts as the origin of shatter cones. *Nature*, *418*(6895), 310-313.
Schenk, P.M., 1993. Central pit and dome craters: Exposing the interiors of Ganymede and Callisto. Journal of Geophysical Research: Planets 98, 7475–7498. https://doi.org/10.1029/93JE00176
Schmieder, M., Kring, D.A., 2020. Earth's Impact Events Through Geologic Time: A List of Recommended Ages for Terrestrial Impact Structures and Deposits. Astrobiology 20, 91–141. https://doi.org/10.1089/ast.2019.2085
Schmieder, M., Jourdan, F., 2013. The Lappajärvi impact structure (Finland): Age, duration of crater cooling, and implications for early life. *Geochimica et Cosmochimica Acta*, *112*, 321-339.

Sharpton, V.L., 2014. Outcrops on lunar crater rims: Implications for rim construction mechanisms, ejecta volumes and excavation depths. Journal of Geophysical Research: Planets 119, 154–168. https://doi.org/10.1002/2013JE004523
Shoemaker, E.M., 1963. Impact Mechanics at Meteor Crater, Arizona. The Moon Meteorites and Comets 301.
Shoemaker, E.M., Batson, R.M., Holt, H.E., Morris, E.C., Rennilson, J.J., Whitaker, E.A., 1969. Observations of the lunar regolith and the Earth from the television camera on Surveyor 7. Journal of Geophysical Research (1896-1977) 74, 6081–6119. https://doi.org/10.1029/JB074i025p06081
Steinbrügge, G., Voigt, J.R., Wolfenbarger, N.S., Hamilton, C.W., Soderlund, K.M., Young, D.A., Blankenship, D.D., Vance, S.D. and Schroeder, D.M., 2020. Brine migration and impact-induced cryovolcanism on Europa. *Geophysical Research Letters*, *47*(21), p.e2020GL090797.
Stewart, S.T., 2020. Equation of State Model Iron ANEOS: Documentation and Comparisons (Version SLVTv0.2G1). Zenodo. http://doi.org/10.5281/zenodo.3866507
Stewart, S.T., Leinhardt, Z.M. (2009). Velocity-dependent catastrophic disruption criteria for planetesimals. *The Astrophysical Journal*, *691*(2), L133.
Stöffler, D., 1984. Glasses formed by hypervelocity impact. Journal of Non-Crystalline Solids, Proceedings of the International Conference on Glass in Planetary and Geological Phenomena 67, 465–502. https://doi.org/10.1016/0022-3093(84)90171-6
Stöffler, D., Hamann, C., Metzler, K., 2018. Shock metamorphism of planetary silicate rocks and sediments: Proposal for an updated classification system. Meteoritics & Planetary Science 53, 5–49. https://doi.org/10.1111/maps.12912
Stöffler, D., Langenhorst, F., 1994. Shock metamorphism of quartz in nature and experiment: I. Basic observation and theory*. Meteoritics 29, 155–181. https://doi.org/10.1111/j.1945-5100.1994.tb00670.x
Sturm, S., Kenkmann, T., Hergarten, S., 2016. Ejecta thickness and structural rim uplift measurements of Martian impact craters: Implications for the rim formation of complex impact craters. Journal of Geophysical Research: Planets 121, 1026–1053. https://doi.org/10.1002/2015JE004959
Timms, N.E., Kirkland, C.L., Cavosie, A.J., Rae, A.S.P., Rickard, W.D.A., Evans, N.J., Erickson, T.M., Wittmann, A., Ferrière, L., Collins, G.S., Gulick, S.P.S., 2020. Shocked titanite records Chicxulub hydrothermal alteration and impact age. Geochimica et Cosmochimica Acta 281, 12–30. https://doi.org/10.1016/j.gca.2020.04.031
Wahl, D., Wieczorek, M. A., Wünnemann, K., & Oberst, J. (2020). Crustal porosity of lunar impact basins. *Journal of Geophysical Research: Planets*, *125*(4), e2019JE006335.
Ward, W.R. and Rudy, D.J., 1991. Resonant obliquity of Mars?. *Icarus*, *94*(1), pp.160-164.
Wieczorek, M.A., Neumann, G.A., Nimmo, F., Kiefer, W.S., Taylor, G.J., Melosh, H.J., Phillips, R.J., Solomon, S.C., Andrews-Hanna, J.C., Asmar, S.W., Konopliv, A.S., Lemoine, F.G., Smith, D.E., Watkins, M.M., Williams, J.G., Zuber, M.T., 2013. The Crust of the Moon as Seen by GRAIL. Science 339, 671–675. https://doi.org/10.1126/science.1231530
Wieczorek, M.A., Weiss, B.P., Stewart, S.T., 2012. An Impactor Origin for Lunar Magnetic Anomalies. Science 335, 1212–1215. https://doi.org/10.1126/science.1214773
Wieland, F., Reimold, W.U., Gibson, R.L. (2006). New observations on shatter cones in the Vredefort impact structure, South Africa, and evaluation of current hypotheses for shatter cone formation. *Meteoritics & Planetary Science*, *41*(11), 1737-1759.
Wiggins, S.E., Johnson, B.C., Bowling, T.J., Melosh, H.J., Silber, E.A., 2019. Impact Fragmentation and the Development of the Deep Lunar Megaregolith. Journal of Geophysical Research: Planets 124, 941–957. https://doi.org/10.1029/2018JE005757

Wünnemann, K., Collins, G.S., Osinski, G.R., 2008. Numerical modelling of impact melt production in porous rocks. Earth and Planetary Science Letters 269, 530–539. https://doi.org/10.1016/j.epsl.2008.03.007

Yue, Z., Di, K., Liu, Z., Michael, G., Jia, M., Xin, X., Liu, B., Peng, M., Liu, J., 2019. Lunar regolith thickness deduced from concentric craters in the CE-5 landing area. Icarus 329, 46–54. https://doi.org/10.1016/j.icarus.2019.03.032